Magnetized Laser-Plasma Interactions in High-Energy-Density Systems: Parallel Propagation

E. E. Los[1] and D. J. Strozzi[2]
[1)]*Physics Department, Imperial College London, South Kensington Campus, London SW7 2AZ*
[2)]*Lawrence Livermore National Laboratory, Livermore, CA, 94551, USA*

(Dated: 2 November 2021)

We investigate parametric processes in magnetised plasmas, driven by a large-amplitude pump light wave. Our focus is on laser-plasma interactions relevant to high-energy-density (HED) systems, such as the National Ignition Facility and the Sandia MagLIF concept. We derive dispersion relations for three-wave interactions in a multi-species plasma using Maxwell's equations, the warm-fluid momentum equation and the continuity equation. The application of an external B field causes right and left polarised light waves to propagate with differing phase velocities. This leads to Faraday rotation of the polarisation, which can be significant in HED conditions. Raman and Brilllouin scattering have modified spectra due to the background B field, though this effect is usually small in systems of current practical interest. We identify a scattering process we call stimulated whistler scattering, where a light wave decays to an electromagnetic whistler wave ($\omega \lesssim \omega_{ce}$) and a Langmuir wave. This only occurs in the presence of an external B field, which is required for the whistler wave to exist. We compute the scattered wavelengths for Raman, Brillouin, and whistler scattering.

arXiv:2111.00224v1 [physics.plasm-ph] 30 Oct 2021

I. INTRODUCTION

Imposing a magnetic field on HED systems is a topic of much current interest. This has several motivations, including reduced electron thermal conduction to create hotter systems (such as for x-ray sources[1]), laboratory astrophysics[2], and magnetised inertial confinement fusion (ICF) schemes. If successful, they could provide efficient, low-cost alternatives to unmagnetised, laser-driven ICF. In the most successful case, the Sandia MagLIF concept [3,4], an external axial magnetic field is used to magnetise the deuterium-tritium (DT) gas contained within a cylindrical conducting liner. A pulsed-power machine then discharges a high current through the liner, generating a Lorentz force which causes the liner to implode. The DT fuel is pre-heated by a laser as the implosion alone is not sufficient to heat the fuel to the ignition temperature. The magnetic field is confined within the liner and hence obeys the MHD frozen in law, which states

$$B_z \pi r^2 = c \tag{1}$$

where r is the radius of the cylindrical liner, B_z is the axial magnetic field and c is a constant. Over the course of the implosion, the magnetic field strength perpendicular to the direction of compression increases as $1/r^2$. Thus, following the implosion, the magnetic field traps fusion alpha particles and thermal electrons, insulating the target and aiding ignition.

The MagLIF scheme, as well as magnetised laser-driven ICF[5,6], motivate us to consider magnetised laser-plasma interactions (LPI), specifically parametric scattering processes[7]. Parametric coupling involves the decay of a large-amplitude or "pump" wave into two or more daughter waves. We focus on those involving one electromagnetic (e/m) and one electrostatic (e/s) daughter wave. In order for parametric coupling to occur, the following frequency and wave-vector matching conditions must be met:

$$\omega_0 = \omega_1 + \omega_2 \tag{2}$$

$$\vec{k}_0 = \vec{k}_1 + \vec{k}_2 \tag{3}$$

where the subscripts 0, 1 and 2 denote the pump, scattered and plasma waves, respectively. Equations 2 and 3 are required by energy and momentum conservation, respectively. Parametric processes can give rise to resonant modes which grow exponentially in the plasma and remove energy from the target[8]. Additionally, light waves which are back-scattered through the optics of the experiment can cause significant damage and even be re-amplified[9–11]. Finally, electron plasma waves can generate superthermal or "hot" electrons which can pre-heat the fuel, thereby increasing the work required to compress it[12].

Laser-driven parametric processes have been extensively researched in unmagnetised plasmas. However, the advent of experiments such as MagLIF and the possibility of magnetised experiments on the National Ignition Facility (NIF)[13–15] necessitate re-examining the impact of a magnetic field on them, which is usually neglected. This is not unexplored territory. For instance, prior work studied how an external axial B field affects Raman backscattering in a hot, inhomogeneous plasma[16], and the decay of circularly polarised EM waves in cold, homogeneous plasma[17]. Recently, excellent theoretical work on a warm-fluid model for magnetized LPI has been done by Shi[18]. Winjum et al.[19] have studied SRS in a magnetized plasma with a particle-in-cell code in conditions relevant to indirect-drive ICF. This work focuses on how the B field affects large-amplitude Langmuir waves, which can nonlinearly trap resonant electrons and modify the Landau damping. Our work ignores nonlinearity and damping, both of which are important in real systems.

Besides modifying existing processes, a background B field gives rise to new waves, one of which is an electromagnetic "whistler" wave which has $\omega \leq \omega_{ce}$, the electron cyclotron frequency. Thus, a plethora of new parametric processes involving this wave can occur, including one which we call "stimulated whistler scattering", in which the pump light wave decays to an electrostatic Langmuir wave and a whistler wave. Parametric processes involving whistlers have been known for some time. For instance, a collection of new instabilities (mostly involving whistler waves) which include

purely growing, modulational and beat-wave instabilities in hot, inhomogeneous plasmas has been explored by Forslund et al.[20]. The decay of a high-frequency whistler wave into a Bernstein wave and a low-frequency whistler wave in hot, inhomogeneous plasmas have also been investigated[21]. Additionally, parametric decays involving three whistler waves in cold, homogeneous plasmas have been studied[22]. In magnetized fusion, parametric interactions of large-amplitude RF waves launched by external antennas, for plasma heating and current drive, have been explored since the 1970s.[23]

This paper aims to present the theory of magnetized LPI in a self-contained way, for a simple enough situation where that is feasible. Namely, we consider all wavevectors parallel to the background B field, and use warm-fluid theory with multiple ion species. The results are mostly special cases of prior ones, especially by Shi, but we hope the reader benefits from a relatively simple presentation. We obtain a parametric dispersion relation, meaning one where the pump light wave is included in the equilibrium, in the spirit of Drake et al.[24]. We then study the "kinematics" of magnetized three-wave interactions, based on phase-matching, in HED-relevant conditions (e.g. for NIF and MagLIF). We consider magnetized modifications to stimulated Raman and Brillouin scattering, as well as stimulated whistler scattering.

The rest of the paper is organized as follows. In section 2, we use the warm-fluid equations to derive the parametric dispersion relation. These are then linearized and decomposed in Fourier modes. Only resonant terms satisfying phase-matching are retained. In section 3, the resulting free-wave dispersion relations in a magnetised and unmagnetised plasma are discussed, along with the Faraday rotation of light-wave polarization. Section 4 studies the impact of the external magnetic field on stimulated Raman and Brillouin scattering in typical HED plasmas. Stimulated whistler scattering is also explored. Section 5 concludes and discusses future prospects.

II. PARAMETRIC DISPERSION RELATIONS FOR MAGNETISED PLASMA WAVES

This section develops a parametric dispersion relation, meaning one where the pump is included in the equilibrium. This approach is in the spirit of the paper by Drake[24] for kinetic, unmagnetised plasma waves, and also for magnetised waves[25]. Subsequent kinetic work was done which extended the Drake approach to include a background B field[26,27]. While our approach does not contain new results compared to the latter, we believe it is useful to work through the details explicitly - especially in a form familiar to the unmagnetised LPI community. The upshot of the lengthy math is Eq. 67, which the reader should understand in physical terms before delving into the details of this section. Our goal is expressions for the amplitude-independent D's (which give linear dispersion relations) and Δ's (which give parametric coupling).

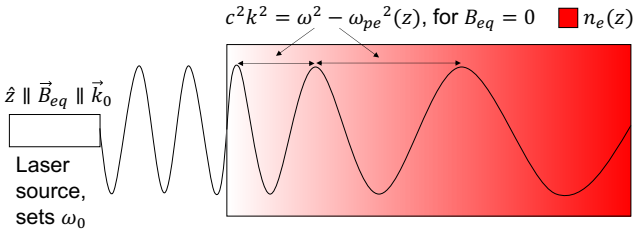


FIG. 1: Geometry of the experimental setup considered throughout the paper. The pump frequency, ω_0, is set by the laser. An external magnetic field, $B_{eq}\hat{z}$, is imposed parallel to the propagation direction of the laser, $\hat{k}_0$. The laser is incident from vacuum on a plasma with density, n_e, which varies with z. The wave vector is therefore also z dependent.

A. Governing Equations

The subscript s will be used to denote species, with mass m_s and charge $q_s = Z_s e$ ($e > 0$ the positron charge). The subscript j will denote the wave or mode. We start with the 3D, non-relativistic Vlasov-Maxwell system with no collisions, and assume spatial variation only in the z direction. Hence, all vectors directed along $\hat{z}$ are longitudinal, and all vectors which lie in the x-y plane are transverse. An experimental configuration for which these assumptions hold is shown in figure 1. We further assume that the distribution function for species s, f_s (particles per $dz * d^3w$, where $\vec{w}$ denotes velocity, and we have integrated over x and y) can be written in a separable form: $f_s(t,z,\vec{w}) = f_{s\perp}(t,z,\vec{w}_\perp)F_s(t,z,w_z)$. $f_{s\perp}$ allows for transverse electromagnetic waves, and is normed such that $\int f_{s\perp} d^2w_\perp = 1$. F_s is the 1D distribution (particles per $dz * dw_z$). Standard manipulations lead to the following 1D Vlasov-Maxwell system:

$$\partial_t F_s + w_z \partial_z F_s = -\frac{q_s}{m_s}(E_z + (\vec{v}_s \times \vec{B})_z)\partial_{w_z} F_s \tag{4}$$

$$(\partial_t + v_{sz}\partial_z)\vec{v}_{s\perp} = \frac{q_s}{m_s}(\vec{E}_\perp + (\vec{v}_s \times \vec{B})_\perp) \tag{5}$$

$$\begin{aligned} &n_s = \int F_s \mathrm{d}w_z, \quad \vec{v}_{s\perp} = \int f_{s\perp}\vec{w}_\perp \mathrm{d}^2 w_\perp, \\ &v_{sz} = n_s^{-1}\int F_s w_z \mathrm{d}w_z \end{aligned} \tag{6}$$

$$B_z = B_{eq} = \text{const} \tag{7}$$

$$\partial_t \vec{B}_\perp = \partial_z(E_y, -E_x) \tag{8}$$

$$\partial_t \vec{E}_\perp = c^2 \partial_z(-B_y, B_x) - \frac{e}{\varepsilon_0}\sum_s Z_s n_s \vec{v}_{s\perp} \tag{9}$$

$$\partial_t E_z = -\frac{e}{\varepsilon_0}\sum_s Z_s n_s v_{sz} \tag{10}$$

$B_{eq} > 0$ and the subscript eq indicates a non-zero, zeroth order background term. Poisson's equation is not listed since the inclusion of Ampere's law and charge continuity render it redundant. It is possible to satisfy Maxwell's equations (equations 8, 9, and 10) by writing $\vec{E}$ and $\vec{B}$ in terms of scalar and vector potentials, ϕ and $\vec{A}$: $\vec{E} = -\vec{\nabla}\phi - \frac{\partial \vec{A}}{\partial t}$ and $\vec{B} = \vec{\nabla} \times \vec{A} + B_{eq}\hat{z}$. We choose the Weyl gauge, in which $\phi = 0$ and $\vec{A} = \vec{A}_\perp + A_z\vec{z}$. Faraday's law is then automatic, and the remaining Maxwell's equations become:

$$\partial_t^2 A_z = \frac{e}{\varepsilon_0} \sum_s Z_s n_s v_{sz} \tag{11}$$

$$(\partial_t^2 - c^2\partial_z^2)\vec{A}_\perp = \frac{e}{\varepsilon_0} \sum_s Z_s n_s \vec{v}_{s\perp} \tag{12}$$

We arrive at fluid equations by taking moments $\int w_z^p \mathrm{d}w_z$ of the equation for F_s, for $p = 0$, 1, and 2:

$$\partial_t n_s + \partial_z(n_s v_{sz}) = 0 \tag{13}$$

$$\partial_t(n_s v_{sz}) + \partial_z\left(n_s v_{sz}^2 + \frac{P_s}{m_s}\right) = \frac{q_s n_s}{m_s}(E_z + (\vec{v}_s \times \vec{B})_z) \tag{14}$$

$$(\partial_t + v_{sz}\partial_z)P_s = -3P_s\partial_z v_{sz} - 2\partial_z Q_s \tag{15}$$

with pressure $P_s \equiv m_s \int F_s(w_z - v_{sz})^2 \mathrm{d}w_z$ and heat flux $Q_s \equiv (m_s/2)\int F_s(w_z - v_{sz})^3 \mathrm{d}w_z$. Note that the pressure is the zz component of the 3D pressure tensor, *not* the scalar, isotropic pressure. We can close the fluid-moment system by replacing the pressure equation with a polytrope equation of state, where K_s is a constant:

$$P_s = n_s T_s = K_s n_s^{\gamma_s} \tag{16}$$

$$\partial_z P_s = K_s \gamma_s n_s^{\gamma_s - 1}\partial_z n_s = \gamma_s T_s \partial_z n_s \tag{17}$$

Common choices for linearised dynamics are isothermal ($\gamma_s = 1$) and adiabatic ($\gamma_s = 3$), which follows from setting $Q_s = 0$ in the pressure equation. Let us recap the complete fluid-Maxwell system, with the substitutions $\vec{a} = \frac{e}{m_e}\vec{A}$ (units of speed), $\omega_{ps}^2 = \frac{q_s^2 n_{seq}}{\varepsilon_0 m_s}$, $\omega_{cs} = |\frac{q_s}{m_s}B_{eq}|$, $\mu_s = \frac{m_s}{m_e Z_s}$ and $s_s = -1, 1$ for electrons and ions respectively:

$$\partial_t^2 a_z - \sum_s \omega_{ps}^2 \mu_s \frac{n_s}{n_{seq}} v_{sz} = 0 \tag{18}$$

$$(\partial_t^2 - c^2\partial_z^2)\vec{a}_\perp = \sum_s \omega_{ps}^2 \mu_s \frac{n_s}{n_{seq}} \vec{v}_{s\perp} \tag{19}$$

$$\partial_t v_{sz} + \mu_s^{-1}\partial_t a_z + v_{sz}\partial_z v_{sz} + \gamma_s \frac{T_s}{m_s n_s}\partial_z n_s = \mu_s^{-1}\vec{v}_{s\perp} \cdot \partial_z \vec{a}_\perp \tag{20}$$

$$\partial_t \vec{v}_{s\perp} + \mu_s^{-1}\partial_t \vec{a}_\perp - s_s \omega_{cs}\vec{v}_{s\perp} \times \hat{z} = -\mu_s^{-1} v_{sz}\partial_z \vec{a}_\perp - v_{sz}\partial_z \vec{v}_{s\perp} \tag{21}$$

$$\partial_t n_s + \partial_z(n_s v_{sz}) = 0 \tag{22}$$

Terms that can give rise to parametric couplings of interest have been moved to the RHS. These involve at least one e/m wave, which will become the pump, and one e/m or e/s wave, which will become one of the daughters. All other terms have been moved to the LHS, namely those that are purely linear or contain 2nd-order terms not of interest. It is clear that the longitudinal dynamics are unaffected by B_{eq} in the absence of parametric coupling, since we chose $\vec{k}||B_{eq}\hat{z}$.

B. Linearisation: Physical Space

We consider parametric processes involving the decay of a fixed, finite-amplitude, electromagnetic pump to an electromagnetic and an electrostatic daughter wave, denoted by subscripts 0, 1 and 2, respectively. The daughter waves are assumed to be much lower in amplitude than the pump. We write the velocity and vector potential pertaining to each wave as an infinite sum of terms of increasing order in amplitude. We neglect all terms of second-order or higher in the pump amplitude (such as the ponderomotive term, which scales as a_0^2), retaining only terms which are strictly linear in wave amplitudes or involve the product of one pump and one daughter amplitude. The plasma density is approximated by the sum of a static, uniform equilibrium term, n_{seq} and a perturbation induced by the electrostatic wave, n_{s2}. We assume that no background flows exist in the plasma ($v_{seq} = 0$), no external electric fields are imposed upon it ($a_{eq} = 0$), and quasi-neutrality holds ($\sum_s q_s n_{seq} = 0$). We write

$$\vec{a}_\perp = \vec{a}_{0\perp} + \vec{a}_{1\perp} \tag{23}$$

$$a_z = a_2 \tag{24}$$

$$\vec{v}_{s\perp} = \vec{v}_{s0\perp} + \vec{v}_{s1\perp} \tag{25}$$

$$v_{sz} = v_{s2} \tag{26}$$

$$n_{sz} = n_{seq} + n_{s2} \tag{27}$$

where $\vec{a}_j$, $\vec{v}_j$ and n_{s2} are functions of t, z. Since we are only interested in second order terms which give rise to parametric coupling, we can linearise equation 17:

$$\frac{\partial_z P_s}{n_s} = \gamma_s \frac{T_{seq}}{n_{seq}}\partial_z n_{s2} \tag{28}$$

Substituting these results and equations 23-27 into equations 18-22 and keeping only coupling terms of interest, we obtain, for waves 1 and 2:

$$\partial_t^2 a_2 - \sum_s \omega_{ps}^2 \mu_s v_{s2} = 0 \tag{29}$$

$$(\partial_t^2 - c^2\partial_z^2)\vec{a}_1 - \sum_s \omega_{ps}^2 \mu_s \vec{v}_{s1} = \sum_s \omega_{ps}^2 \mu_s \frac{n_{s2}}{n_{seq}}\vec{v}_{s0} \tag{30}$$

$$\partial_t v_{s2} + \mu_s^{-1}\partial_t a_2 + \gamma_s \frac{v_{Ts}^2}{n_{seq}}\partial_z n_{s2} = \mu_s^{-1}\left(\vec{v}_{s0}\cdot\partial_z\vec{a}_1 + \vec{v}_{s1}\cdot\partial_z\vec{a}_0\right) \quad (31)$$

$$\partial_t \vec{v}_{s1} + \mu_s^{-1}\partial_t\vec{a}_1 - s_s\omega_{cs}\vec{v}_{s1}\times\hat{z} = -v_{s2}\partial_z(\vec{v}_{s0} + \mu_s^{-1}\vec{a}_0) \quad (32)$$

$$\partial_t n_{s2} + n_{seq}\partial_z v_{s2} = 0 \quad (33)$$

where $v_{Ts}^2 = \frac{T_{eqs}}{m_s}$. The $-v_{sz}\partial_z v_{sz}$ term in equation 20 has been neglected because it is second order in the daughter wave amplitude. Wave 0 satisfies the same eqs. as wave 1 (i.e. Eqs. 30 and 32) without the coupling terms (RHS = 0). For the daughter waves 1 and 2, we now have $2s+1$ scalar and $s+1$ vector equations for $2s+1$ scalar (n_{s2}, v_{s2} and a_2) and $s+1$ vector ($\vec{v}_{s1}$ and $\vec{a}_1$) unknowns, with all vectors in the 2D transverse (xy) plane. Our plan is to move to Fourier space, retain only linear and parametric-coupling terms, and arrive at a closed system just involving the a's.

C. Fourier Decompositions

If the variable X is used to represent the electric field, electron density or wave velocity, then X can be written as a Fourier decomposition, in which j denotes the wave (0,1,2):

$$X_j(t,\vec{r}) = \frac{1}{2}X_{fj}e^{i\psi_j} + cc \quad (34)$$

Subscript f denotes the Fourier amplitude, phase $\psi_j = (\vec{k_j}\cdot\vec{r} - \omega_j t) \equiv k_j z - \omega_j t$ and cc is an abbreviation of complex conjugate. Since all successive amplitudes will be Fourier amplitudes, the subscript f will henceforth be neglected. Wave 1 can be written in terms of two e/m waves, with either an up-shifted or a down-shifted frequency vs. wave 0, denoted by subscripts + and - respectively. The phase matching conditions are hence

$$\psi_- = \psi_0 - \psi_2^* \qquad \psi_+ = \psi_0 + \psi_2 \quad (35)$$

Growth due to parametric coupling means the daughter-wave k_j and ω_j can be complex. It is assumed that the pump amplitude is fixed (no damping or pump depletion), hence k_0 and ω_0 are real, and $\psi_0^* = \psi_0$. We choose our definitions of $\psi_\pm$ so they and ψ_2 have the same imaginary part, i.e. the same parametric growth rate. We also choose all frequencies to have a positive real part: the companion field for $\mathrm{Re}[\omega] < 0$ follows from the condition that the physical field is real. Although one can mix positive and negative frequency waves, we find the analysis simpler with all $\mathrm{Re}[\omega] > 0$. Especially with magnetized waves, the discussion of circular polarization for $\mathrm{Re}[\omega] < 0$ can become confusing.

1. Plasma Waves in Fourier Space

We shall eliminate n_{s2} and $\vec{v}_{s2}$ in favour of the a's. Substituting equation 34 into equations 29 and 33, we obtain:

$$a_2 + \frac{1}{\omega_2^2}\sum_s \omega_{ps}^2\mu_s v_{s2} = 0 \quad (36)$$

and

$$n_{s2} = n_{seq}\frac{k_2}{\omega_2}v_{s2} \quad (37)$$

respectively. Repeating for equation 31 gives:

$$\left(-\frac{\omega_2}{2}v_{s2} - \frac{\mu_s^{-1}}{2}\omega_2 a_2 + \frac{\gamma_s v_{Ts}^2}{2n_{eqs}}k_2 n_{s2}\right) + cc = \frac{\mu_s^{-1}}{4}PC_{s2} + cc \quad (38)$$

where the parametric coupling terms are contained in PC_{s2} (units of frequency*speed), and

$$\begin{aligned} PC_{s2} = -ie^{-i\psi_2}Res_2[&(\vec{v}_{s0}e^{i\psi_0})\cdot(ik_\pm\vec{a}_\pm e^{i\psi_\pm}) \\ &+ (\vec{v}_{s0}e^{i\psi_0})\cdot(-ik_\pm^*\vec{a}_\pm^* e^{-i\psi_\pm^*}) + (\vec{v}_{s\pm}e^{i\psi_\pm})\cdot(ik_0\vec{a}_0 e^{i\psi_0}) \\ &+ (\vec{v}_{s\pm}e^{i\psi_\pm})\cdot(-ik_0^*\vec{a}_0^* e^{-i\psi_0^*}) + cc \end{aligned} \quad (39)$$

where Res_2 denotes terms which are resonant with mode 2. Using equation 37 to substitute for n_{s2}:

$$-\omega_2(v_{s2} + \mu_s^{-1}a_2) + \gamma_s\frac{k_2^2 v_{Ts}^2}{\omega_2}v_{s2} = \frac{\mu_s^{-1}}{2}PC_{s2} \quad (40)$$

Rearranging for v_{s2}:

$$v_{s2} = -\frac{\omega_2 P_s}{\mu_s\omega_{ps}^2}(\omega_2 a_2 + PC_{s2}) \quad (41)$$

$$P_s = \frac{\omega_{ps}^2}{\omega_2^2 - \gamma_s k_2^2 v_{Ts}^2} \quad (42)$$

Substituting this result into equation 36, we obtain:

$$\left(1 - \sum_s P_s\right)a_2 = \frac{1}{2\omega_2}\sum_s P_s PC_{s2} \quad (43)$$

2. EM Waves in Fourier Space

Writing equation 32 in terms of Fourier modes, we obtain:

$$\begin{aligned} &\frac{1}{2}\sum_{+,-}\left(-i\omega_\pm\vec{v}_{s\pm} - i\mu_s^{-1}\omega_\pm\vec{a}_\pm - s_s\omega_{cs}\vec{v}_{s\pm}\times\hat{z}\right)e^{i\psi_\pm} + cc = \\ &-\frac{1}{4}[ik_0 v_{s2}\vec{v}_{s0}e^{i\psi_+} + ik_0 v_{s2}^*\vec{v}_{s0}e^{i\psi_-} \\ &+ \mu_s^{-1}(ik_0 v_{s2}\vec{a}_0 e^{i\psi_+} + ik_0\vec{a}_0 v_{s2}^* e^{i\psi_-})] + cc \end{aligned} \quad (44)$$

Let Z_{y+}, Z_{y-} denote Z_y and Z_y^*, respectively, where Z denotes an amplitude, frequency or wavelength, and y denotes a subscript containing the mode and plasma species (if applicable) of Z. This allows us to write generic equations for the + and - waves. Selecting only resonant terms we obtain:

$$\omega_\pm(\vec{v}_{s\pm} + \mu_s^{-1}\vec{a}_\pm) - is_s\omega_{cs}\vec{v}_{s\pm}\times\hat{z} = \frac{k_0}{2}v_{s2\pm}(\vec{v}_{s0} + \mu_s^{-1}\vec{a}_0) \quad (45)$$

Finally, equation 30, once written in terms of Fourier modes, becomes:

$$\frac{1}{2}\sum_{+,-}\left((-\omega_{\pm}^2+c^2k_{\pm}^2)\vec{a}_{\pm}-\sum_s\omega_{ps}^2\mu_s\vec{v}_{\pm}\right)e^{i\psi_{\pm}}+cc= \sum_s\omega_{ps}^2\frac{\mu_s}{4n_{seq}}(\vec{v}_{s0}n_{s2}e^{i\psi_+}+\vec{v}_{s0}n_{s2}^*e^{i\psi_-})+cc \tag{46}$$

Keeping terms resonant with $\psi_{\pm}$ and eliminating n_{s2} gives

$$(-\omega_{\pm}^2+k_{\pm}^2c^2)\vec{a}_{\pm}-\sum_s\omega_{ps}^2\mu_s\vec{v}_{s\pm}=\frac{1}{2}\frac{k_{2\pm}}{\omega_{2\pm}}\sum_s\omega_{ps}^2\mu_s v_{s2\pm}\vec{v}_{s0} \tag{47}$$

Using equation 41 to eliminate v_{s2} from equations 45 and 47, keeping only terms up to second order we are left with the following equations, where we restate the plasma-wave equation for convenience:

$$\vec{v}_{s\pm}+\mu_s^{-1}\vec{a}_{\pm}-i\beta_{s\pm}\vec{v}_{s\pm}\times\hat{z}=-K_{s\pm}a_{2\pm}(\vec{v}_{s0}+\mu_s^{-1}\vec{a}_0) \tag{48}$$

$$(-\omega_{\pm}^2+k_{\pm}^2c^2)\vec{a}_{\pm}-\sum_s\omega_{ps}^2\mu_s\vec{v}_{s\pm}=-\frac{k_{2\pm}\omega_{2\pm}}{2}\sum_sP_{s\pm}a_{2\pm}\vec{v}_{s0} \tag{49}$$

$$(1-\sum_sP_s)a_2=\frac{1}{2\omega_2}\sum_sP_sPC_{s2} \tag{50}$$

$K_{s\pm}=\frac{k_0\omega_{2\pm}^2P_{s\pm}}{2\mu_s\omega_{\pm}\omega_{ps}^2}$, $\beta_{s\pm}=s_s\frac{\omega_{cs}}{\omega_{\pm}}$ and $P_{s\pm}=\frac{\omega_{ps}^2}{\omega_{2\pm}^2-\gamma_sk_{2\pm}^2v_{Ts}^2}$. $\omega_{2+}=\omega_2$, $\omega_{2-}=\omega_2^*$, and similarly for $k_{2\pm}$. The equations for wave 0 are equivalent to those for the $\pm$ waves, neglecting second order terms.

At this point, the remaining task is to solve for $\vec{v}_{s\pm}$ in terms of $\vec{a}_{\pm}$, a_2, and wave 0 quantities. We will finally arrive at a 5×5 system for $\vec{a}_+$, $\vec{a}_-^*$, and a_2, which includes both the linear waves and parametric coupling to wave 0. For magnetised waves, this is most easily done in a rotating coordinate system, where R and L circularly-polarised waves are the linear light waves.

D. Left-Right Co-ordinate System

It is convenient when dealing with Fourier amplitudes to formulate vectors in terms of right and left polarised coordinates, which are defined in terms of cartesian co-ordinates as follows:

$$\hat{R}=\frac{1}{\sqrt{2}}(\hat{x}+i\hat{y})$$
$$\hat{L}=\frac{1}{\sqrt{2}}(\hat{x}-i\hat{y}) \tag{51}$$

In condensed notation,

$$\hat{\sigma}=\frac{1}{\sqrt{2}}(\hat{x}+i\sigma\hat{y}) \tag{52}$$

where $\sigma=+1,-1$ for the right and left-polarised basis vectors, respectively. We define the dot product such that $\vec{a}\cdot\vec{b}=\sum_i a_ib_i^*$. Thus, dot products do not commute: $\vec{a}\cdot\vec{b}=(\vec{b}\cdot\vec{a})^*$. This normalisation ensures $\hat{\sigma}\cdot\hat{\sigma}=1$. Using this convention, any vector can be re-written in terms of right and left polarised unit vectors and amplitudes. Consider, for example, the physical velocity vector $\vec{v}_{\perp}$, where we explicitly indicate Fourier amplitudes with subscript f:

$$\begin{aligned}\vec{v}_{\perp}&=(\hat{x}v_{fx}+\hat{y}v_{fy})e^{i\psi}+cc\\&=\frac{1}{\sqrt{2}}((\hat{R}+\hat{L})v_{fx}+i(\hat{L}-\hat{R})v_{fy})e^{i\psi}+cc\\&=\frac{1}{\sqrt{2}}(\hat{L}(v_{fx}+iv_{fy})+\hat{R}(v_{fx}-iv_{fy}))e^{i\psi}+cc\\&=\frac{1}{\sqrt{2}}(v_{fL}\hat{L}+v_{fR}\hat{R})e^{i\psi}+cc\\&=e^{i\psi}\sum_{\sigma}v_{f\sigma}\hat{\sigma}+cc\end{aligned} \tag{53}$$

Note that $\vec{v}\cdot\hat{\sigma}=2^{-1/2}e^{i\psi}(v_x-i\sigma v_y)=e^{i\psi}v_{f\sigma}+cc$. As an explicit example, for an R wave with $v_{fR}=V$ real and $v_{fL}=0$, $\vec{v}_{\perp}=2^{1/2}V(\cos\psi,-\sin\psi)$. At fixed z, $\vec{v}_{\perp}$ rotates clockwise as time increases when looking toward $-\hat{z}$, which is opposite to $\vec{B}_{eq}$. We therefore follow the convention used by Stix[28], in which circular polarization is defined relative to $\vec{B}_{eq}$ and not $\vec{k}$.

We use the result given in the last line of equation 53 to produce the definition of a dot product of two vectors in Fourier space in this coordinate system. Consider the vectors $\vec{v}$ and $\vec{a}$:

$$\vec{v}.\vec{a}=e^{i(\psi_i-\psi_j^*)}(v_{fRi}a_{fRj}^*+v_{fLi}a_{fLj}^*)+cc \tag{54}$$

where the subscripts i, j are the wave indices.

E. EM Waves in Left-Right Coordinates

Taking $\hat{\sigma}\cdot$ (equations 48 and 49), we obtain

$$(1+\sigma\beta_{s\pm})v_{s\pm\sigma}+\mu_s^{-1}a_{\pm\sigma}=-K_{s\pm}\left(\mu_s^{-1}a_{0\sigma}+v_{s0\sigma}\right)a_{2\pm} \tag{55}$$

$$(\omega_{\pm}^2-k_{\pm}^2c^2)a_{\pm\sigma}+\sum_s\omega_{ps}^2\mu_sv_{s\pm\sigma}=\frac{k_{2\pm}\omega_{2\pm}}{2}\sum_sP_{s\pm}a_{2\pm}v_{s0\sigma} \tag{56}$$

respectively, where $a_{\pm\sigma}\equiv\vec{a}_{\pm}\cdot\hat{\sigma}$. The definitions of $v_{s\pm\sigma}$, $v_{s0\sigma}$ and $a_{0\sigma}$ are analogous to that of $a_{\pm\sigma}$. We now have uncoupled equations for $(a_{\pm\sigma},v_{s\pm\sigma})$ which is the advantage of using rotating coordinates. This is unlike the original x and y coordinates, which are coupled due to the $\vec{v}\times\vec{B}$ force. For the pump wave, we have these equations with subscript $\pm\to0$ and set the RHS to 0. Thus

$$v_{s0\sigma}=-\frac{1}{\mu_s(1+\sigma\beta_{s0})}a_{0\sigma} \tag{57}$$

Rearranging equation 55 to obtain an expression for $v_{s\pm\sigma}$

$$(1+\sigma\beta_{s\pm})v_{s\pm\sigma}=-\mu_s^{-1}a_{\pm\sigma}-\frac{\sigma K_{s\pm}\beta_{s0}}{\mu_s(1+\sigma\beta_{s0})}a_{0\pm\sigma}a_{2\pm} \tag{58}$$

Substituting this into equation 56, and moving parametric coupling terms to the right-hand side, we obtain:

$$D_{\pm\sigma}a_{\pm\sigma} = -\Delta_{\pm\sigma 2}a_{0\sigma}a_{2\pm} \tag{59}$$

where

$$\begin{aligned} D_{\pm\sigma} &= \omega_{\pm}^2 - k_{\pm}^2c^2 - \sum_s \frac{\omega_{ps}^2}{1+\sigma\beta_{s\pm}} \\ \Delta_{\pm\sigma 2} &= \frac{\omega_{2\pm}}{2}\sum_s \frac{P_{s\pm}}{\mu_s}\frac{1}{1+\sigma\beta_{s0}}\left(k_{2\pm} - k_0\frac{\omega_{2\pm}}{\omega_{\pm}}\frac{\sigma\beta_{s0}}{1+\sigma\beta_{s\pm}}\right) \end{aligned} \tag{60}$$

This has the desired form, where wave amplitudes are written only in terms of a's, not v's. For no B field, all β's are zero, and the parametric coupling coefficient $\Delta_{\pm\sigma 2} \propto k_{2\pm}$, the usual unmagnetised result. To explain the notation, D_{+R} gives the linear dispersion relation for the scattered upshifted R wave, and Δ_{+R2} is the parametric coupling coefficient for that wave and wave 2 (the plasma wave). Please see the parametric dispersion relation Eq. 67 below.

F. Plasma Waves in Left-Right Coordinates

Writing the PC_{s2} term in equation 50 in terms of right and left circularly polarised waves, we obtain:

$$\begin{aligned} PC_{s2} &= -k_-^*(v_{s0R}a_{-R}^* + v_{s0L}a_{-L}^*) + k_0(v_{s-R}^*a_{0R} + v_{s-L}^*a_{0L}) \\ &+ k_+(v_{s0R}^*a_{+R} + v_{s0L}^*a_{+L}) - k_0(v_{s+R}a_{0R}^* + v_{s+L}a_{0L}^*) \end{aligned} \tag{61}$$

Substituting for $\vec{v}_{s0}$ using equation 57, and $\vec{v}_{s\pm}$ using equation 58

$$\begin{aligned} -\mu_s PC_{s2} &= a_{0R}a_{-R}^*\left(\frac{k_0}{1+\beta_{s-}^*} - \frac{k_-^*}{1+\beta_{s0}}\right) + \\ &a_{0L}a_{-L}^*\left(\frac{k_0}{1-\beta_{s-}^*} - \frac{k_-^*}{1-\beta_{s0}}\right) \\ &+ a_{0R}^*a_{+R}\left(-\frac{k_0}{1+\beta_{s+}} + \frac{k_+}{1+\beta_{s0}}\right) \\ &+ a_{0L}^*a_{+L}\left(-\frac{k_0}{1-\beta_{s+}} + \frac{k_+}{1-\beta_{s0}}\right) \end{aligned} \tag{62}$$

Equation 50 can now be written in a more condensed form:

$$D_2a_2 = -\sum_{\sigma}\left(\Delta_{2+\sigma}a_{0\sigma}^*a_{+\sigma} + \Delta_{2-\sigma}a_{0\sigma}a_{-\sigma}^*\right) \tag{63}$$

$$D_2 = 1 - \sum_s P_s \tag{64}$$

$$\Delta_{2+\sigma} = \frac{1}{2\omega_2}\sum_s \frac{P_s}{\mu_s}\left(\frac{k_+}{1+\sigma\beta_{s0}} - \frac{k_0}{1+\sigma\beta_{s+}}\right) \tag{65}$$

$$\Delta_{2-\sigma} = \frac{1}{2\omega_2}\sum_s \frac{P_s}{\mu_s}\left(-\frac{k_-^*}{1+\sigma\beta_{s0}} + \frac{k_0}{1+\sigma\beta_{s-}^*}\right) \tag{66}$$

We now have a plasma-wave relation involving just a's.

G. Parametric Dispersion Relation

Equations 59 (really 4 equations: equation 59 and its complex conjugate for $\sigma = R, L$) and 63 form a system of 5 linear equations, which can be summarised in matrix form:

$$\begin{bmatrix} D_{+R} & 0 & 0 & 0 & \Delta_{+R2}a_{0R} \\ 0 & D_{-R}^* & 0 & 0 & \Delta_{-R2}^*a_{0R}^* \\ 0 & 0 & D_{+L} & 0 & \Delta_{+L2}a_{0L} \\ 0 & 0 & 0 & D_{-L}^* & \Delta_{-L2}^*a_{0L}^* \\ \Delta_{2+R}a_{0R}^* & \Delta_{2-R}a_{0R} & \Delta_{2+L}a_{0L}^* & \Delta_{2-L}a_{0L} & D_2 \end{bmatrix} \begin{bmatrix} a_{+R} \\ a_{-R^*} \\ a_{+L} \\ a_{-L^*} \\ a_2 \end{bmatrix} = 0 \tag{67}$$

The structure of this matrix matches our physical understanding of plasma-wave dispersion relations: the diagonal terms are independent of a, and give rise to linear waves. The off-diagonal terms are all proportional to a_0 and represent parametric coupling between the two daughter waves, one e/m and the e/s plasma wave. Nonzero solutions exist when the determinant is zero, which gives the parametric dispersion relation including the pump light wave in the equilibrium. This is analogous to Drake[24], but generalized to include a background magnetic field, and specialized to our 1D geometry and fluid instead of kinetic plasma-wave response.

The parametric dispersion relation couples a pump and scattered e/m wave of the same R or L polarization. Consider the case where there is only one pump wave: i.e. either $a_{0R} = 0$ or $a_{0L} = 0$. Taking $a_{0R} = 0$ for definiteness, waves a_{-R} and a_{-R}^* decouple from the dispersion relation, leaving the following dispersion matrix:

$$\begin{bmatrix} D_{+L} & 0 & \Delta_{+L2}a_{0L} \\ 0 & D_{-L}^* & \Delta_{-L2}^*a_{0L}^* \\ \Delta_{2+L}a_{0L}^* & \Delta_{2-L}a_{0L} & D_2 \end{bmatrix} \begin{bmatrix} a_{+L} \\ a_{-L}^* \\ a_2 \end{bmatrix} = 0 \tag{68}$$

Setting the determinant to 0 gives

$$D_{+L}D_{-L}^*D_2 = |a_{0L}|^2(D_{+L}\Delta_{2-L}\Delta_{-L2}^* + D_{-L}^*\Delta_{2+L}\Delta_{+L2}) \tag{69}$$

$a_{0L} = 0$ then gives the three linear dispersion relations for the upshifted L, downshifted L, and plasma waves: $D_{+L} = 0$, $D_{-L} = 0$, or $D_2 = 0$. $a_{0L} \neq 0$ couples the linear waves and gives parametric interaction.

III. IMPACT OF EXTERNAL B FIELD ON FREE WAVES

This section considers the linear or free waves, with $a_0 = 0$. Let a_1 be either a_+ or a_- in equation 67 to obtain the free-wave dispersion relation:

$$\begin{bmatrix} D_{1L}^* & 0 & 0 \\ 0 & D_{1R}^* & 0 \\ 0 & 0 & D_2 \end{bmatrix} \begin{bmatrix} a_{1L}^* \\ a_{1R}^* \\ a_2 \end{bmatrix} = 0 \tag{70}$$

$\vec{a} \neq 0$ solutions exist if the determinant of this matrix equals 0. This gives rise to the following dispersion relations, for a single ion species. For the e/m waves, with $a_2 = 0$, we have $D_{1L}D_{1R} = 0$, which gives

$$\omega_1^2 = k_1^2c^2 + \frac{\omega_{pe}^2}{1-\sigma\frac{\omega_{ce}}{\omega_1}} + \frac{\omega_{pi}^2}{1+\sigma\frac{\omega_{ci}}{\omega_1}} \tag{71}$$

For e/s waves, with $a_{1L} = a_{1R} = 0$, we have $D_2 = 0$ and

$$\omega_2^2 = \frac{\omega_{pe}^2}{1 - \gamma_e \frac{k_2^2 v_{Te}^2}{\omega_2^2}} + \frac{\omega_{pi}^2}{1 - \gamma_i \frac{k_2^2 v_{Ti}^2}{\omega_2^2}} \tag{72}$$

Note that the background B field has no effect at all on the e/s waves, for our geometry of $\vec{k} || \vec{B}_{eq}$.

A. Waves in an unmagnetised Plasma

By setting $\omega_{ce} = 0$, we recover the unmagnetised dispersion relation for electromagnetic waves from equation 71:

$$\omega_1^2 = c^2 k_1^2 + \omega_{pe}^2 + \omega_{pi}^2 \tag{73}$$

The ion contribution is usually negligible. Equation 72 gives the electrostatic waves, with the conventional approximations, like neglecting ions for electron plasma waves (EPWs), being highly accurate. Namely, we find the EPW for $\gamma_e = 3$:

$$\omega_2^2 = \omega_{pe}^2 + 3 v_{Te}^2 k_2^2 \tag{74}$$

and the ion acoustic wave (IAW) for $\gamma_e = 1, \gamma_i = 3$:

$$\omega_2^2 = \frac{Z_i T_e}{m_i} \left(\frac{1}{1 + (k_2 \lambda_{De})^2} + \frac{3 T_i}{Z_i T_e} \right) k_2^2 \tag{75}$$

with $\lambda_{De} \equiv v_{Te}/\omega_{pe}$. We must retain finite T_e for an IAW to exist.

B. Waves with Magnetic Field

The dispersion relation for free electromagnetic waves in a magnetised plasma is given in equation 71. As is usual in LPI literature, we view this as giving ω as a function of real k. This gives a 4th order polynomial for ω with four real solutions, each of which corresponds to an e/m wave:

$$\begin{aligned} &\omega^4 - \sigma(\omega_{ce} - \omega_{ci})\omega^3 - (c^2 k^2 + \omega_{ce}\omega_{ci} + \omega_{pe}^2 + \omega_{pi}^2)\omega^2 \\ &+ \sigma(\omega_{ce} - \omega_{ci}) c^2 k^2 \omega + \omega_{ce}\omega_{ci} c^2 k^2 = 0 \end{aligned} \tag{76}$$

Note one can solve this trivially in closed form for k given ω. In the following analysis, but not in the numerical solutions, we assume $Z_i m_e/m_i \ll 1$, so we can drop ω_{pi}^2 and set $\omega_{ce} - \omega_{ci} \to \omega_{ce}$. In order of descending frequency, these waves are: the right and left-polarised light waves, the whistler wave and the ion cyclotron wave (ICW). In addition to these waves, two electrostatic waves are obtained by solving equation 72: the EPW and the IAW.

Let us consider the high-frequency e/m waves, the light and whistler waves, where ion motion can be neglected: $\omega_{ci} \to 0$. In this case, equation 76 becomes (removing one $\omega = 0$ root)

$$\omega^3 - \sigma\omega_{ce}\omega^2 - (c^2 k^2 + \omega_{pe}^2)\omega + \sigma\omega_{ce} c^2 k^2 = 0 \tag{77}$$

We assume $\omega_{pe} \gg \omega_{ce}$, which is typical in the HED regime. For light waves, we consider equation 77 for $\omega \gg \omega_{ce}$. For $k = 0$, we find

$$\omega(k=0) \approx \omega_{pe} + \frac{\sigma}{2}\omega_{ce} \tag{78}$$

For all k we write ω as $\omega(B_{eq} = 0) \equiv (c^2 k^2 + \omega_{pe}^2)^{1/2}$ plus a correction:

$$\omega \approx \omega(B_{eq} = 0) + \frac{\sigma}{2} \frac{\omega_{pe}^2}{\omega(B_{eq} = 0)^2} \omega_{ce} \tag{79}$$

Whistler wave: We can also solve equation 77 for the whistler wave, which has $\omega \leq \omega_{ce}$. We call this full set of roots for ω the whistler, though some authors only use this term for the small k domain and use "electron cyclotron wave" when ω is near ω_{ce}. We derive expressions for this wave by considering two limits: first, for $k \to 0$ (but still large enough that we can neglect ion motion, discussed below), we obtain:

$$\omega \approx \sigma \frac{c^2 k^2}{\omega_{pe}^2} \omega_{ce} \tag{80}$$

We restrict interest to $\omega > 0$ waves, which for the whistler requires the R wave ($\sigma = 1$):

$$\omega \approx \frac{c^2 k^2}{\omega_{pe}^2} \omega_{ce} \qquad \sigma = 1 \tag{81}$$

Secondly, for $ck \gg \omega_{pe}$, we obtain:

$$\omega \approx \omega_{ce} \left(1 - \frac{\omega_{pe}^2}{c^2 k^2} \right) \qquad \sigma = 1 \tag{82}$$

For ω near ω_{ce}, the whistler group velocity $d\omega/dk$ approaches zero. Since this is the relevant wave propagation speed for three-wave interactions, such a localized whistler wavepacket would propagate very slowly. This impacts how stimulated whistler scattering evolves, and how to practically realize the process in experiments or simulations.

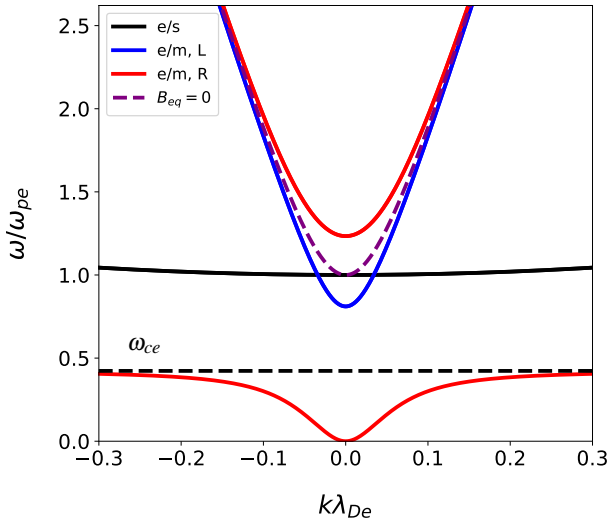
The full numerical solutions of the dispersion relations for the whistler wave and the right and left-polarised light waves are shown in figure 2a. Note that here and throughout the rest of the paper, λ_{De} is used to normalise k, as is customary for stimulated scattering. For large $k\lambda_{De}$, the whistler wave tends to $\omega = \omega_{ce}$, shown in figure 2a as a dashed black line.

Ion cyclotron wave: We now consider the ion cyclotron wave (ICW) which requires the retention of terms involving ion motion. As with the whistler wave, we consider two regimes. For $k \to 0$, we seek solutions with $\omega \propto k$, which gives

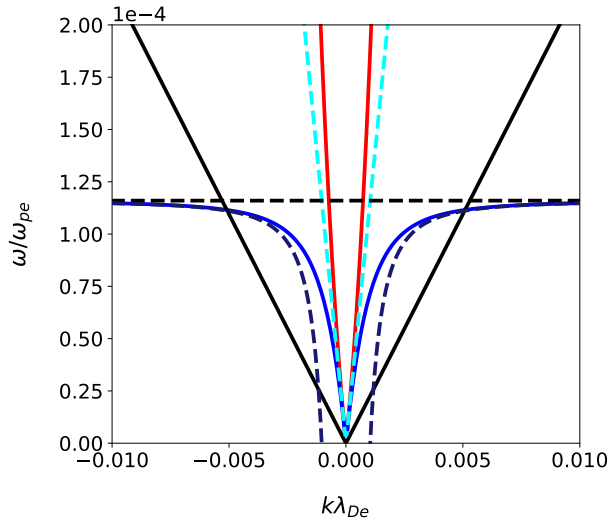
$$\omega \approx v_A k \qquad \sigma = -1 \text{ or } +1 \tag{83}$$

where the Alfven velocity, $v_A = c\frac{\omega_{ci}}{\omega_{pi}} = B/(\rho\mu_0)^{1/2}$. This solution applies for both values of σ, meaning there is both an R wave (the whistler, including ion motion), and an L wave (the ICW). To see which is which, we need to take the opposite limit $ck \gg \omega_{pe}$, where we obtain two solutions with ω independent of k: $\omega = \omega_{ce}$ for $\sigma = 1$ (the right-polarised whistler), and $\omega = \omega_{ci}$ for $\sigma = -1$ (the left-polarised ICW). Including the next correction term for the ICW gives

$$\omega \approx \omega_{ci} \left(1 - \frac{\omega_{pi}^2}{c^2 k^2} \right) \qquad \sigma = 1 \tag{84}$$



(a)



(b)

FIG. 2: Numerical solutions to the free-wave dispersion relations in a magnetized plasma, for the conditions in Table I. Red: right-polarised e/m, blue: left-polarised e/m, purple: unmagnetised e/m, and black: electrostatic. Top: high-frequency waves, in decreasing order: e/m light, electron plasma, and whistler. The black dashed line lies at $\frac{\omega_{ce}}{\omega_{pe}}$. Bottom low-frequency waves: electrostatic ion acoustic wave, right-polarised whistler, and left-polarised ion cyclotron waves. Also plotted are the analytic approximations to the ion cyclotron wave for $ck \gg \omega_{pe}$ (dark blue) (equation 84), which tends to $\frac{\omega_{ci}}{\omega_{pe}}$ (dashed black line), and $k \to 0$, which yields the Alfven frequency (dashed cyan line), given in equation 83.

Figure 2a is re-plotted in figure 2b for $\omega \ll \omega_{pe}$ to show the IAW and ICW clearly. The ICW tends to $\omega = \omega_{ci}$, denoted by a dashed black line. The numerical and approximate analytic solutions to the ICW dispersion relation are shown in figure 2b in blue and dark blue respectively. As can be seen from equation 83, at low $k\lambda_{De}$ the ICW approaches the Alfven frequency, which is represented by a dashed cyan line in figure 2b. For large values of $k\lambda_{De}$, the ICW frequency tends to ω_{ci}, marked by a dashed black line. The parameters used to plot the dispersion relations shown in figures (2a-2b) are given in table I. A plasma comprised of helium ions and electrons was considered.

Quantity	Value
Z	2
A	4
T_e	2 keV
T_i	1 keV
$\frac{\omega_{ce}}{\omega_{pe}}$	0.423

TABLE I: Parameters used to plot dispersion relations.

Laser wavelength [μm]	n_e/n_{crit}	n_e [cm^{-3}]	B_{eq} [T]
0.351 (NIF)	0.15	1.36×10^{21}	5000
0.351	0.01	9.05×10^{19}	1290
10.6 (CO2)	0.15	1.49×10^{18}	166
10.6	0.01	9.92×10^{16}	42.7

TABLE II: Electron densities and magnetic field strengths which correspond to the normalised parameters considered throughout this paper, for typical NIF and CO2 laser wavelengths. $\frac{\omega_{ce}}{\omega_{pe}} = 0.423$ in all cases.

C. Faraday Rotation

Three unique waves exist in an unmagnetised plasma, of which two are electrostatic (the electron plasma wave, (EPW) and the ion acoustic wave, (IAW)) and one is electromagnetic (light wave, with two degenerate polarisations). If the electromagnetic wave is linearly polarised, it can be written as the sum of two circularly polarised waves of equal amplitude and opposite handedness (R and L waves). If an external B field, $\vec{B_{eq}}$ is applied, the R and L waves experience different indices of refraction and propagate with differing phase velocities. Consequently, the overall polarisation of the electromagnetic wave, found by summing the R and L waves, rotates as the electromagnetic wave propagates through the plasma. This is the well-known Faraday effect, which is briefly derived below.

An expression for the wavenumber of the electromagnetic wave can be obtained by rearranging equation 71.

$$k_\sigma = \frac{\omega}{c}\left(1 - \frac{\omega_{pe}^2}{\omega^2(1 - \sigma\frac{\omega_{ce}}{\omega})}\right)^{\frac{1}{2}} \tag{85}$$

Two first-order Taylor expansions of equation 85, assuming $\omega \gg \omega_{ce}$, and $\omega \gg \omega_{pe}$ yield:

$$k_\sigma \approx K - \sigma\Delta K \tag{86}$$

where

$$K = \frac{\omega}{c}\left(1 - \frac{\omega_{pe}^2}{2\omega^2}\right), \qquad \Delta K = \frac{\omega_{pe}^2}{2\omega^2}\frac{\omega_{ce}}{c} \tag{87}$$

Consider a linearly polarised plane electromagnetic wave. We can write the physical electric field $\vec{E} = Re[\vec{E}_F]$ as the sum of the electric fields of two circularly polarised waves with opposite handedness:

$$\vec{E}_F = \varepsilon(\hat{R}e^{i\psi_R} + \hat{L}e^{i\psi_L}) \qquad \psi_{R,L} \equiv k_{R,L}z - \omega t \tag{88}$$

Writing this in Cartesian co-ordinates,

$$\frac{2^{1/2}}{\varepsilon}\vec{E}_F = \hat{x}(e^{i\psi_L} + e^{i\psi_R}) + i\hat{y}(e^{i\psi_L} - e^{i\psi_R}) \tag{89}$$

Assuming ε is real,

$$\begin{aligned} \vec{E} &= E(\cos\phi, -\sin\phi) \\ E &= |2^{1/2}\varepsilon\cos[(1/2)(k_L + k_R)z - \omega t]| \\ \phi &= \frac{1}{2}(k_L - k_R)z = \Delta K z \end{aligned} \tag{90}$$

At a fixed z, $\vec{E}$ always lies along the same line in the xy plane, with its exact position varying in time. As z varies, the angle ϕ this line makes with respect to the x axis increases at the rate

$$\frac{\partial\phi}{\partial z} = \Delta K = 16.8\frac{n_e}{n_{crit}}B_{eq}[\mathrm{T}]\ [\mathrm{deg/mm}] \tag{91}$$

The final formula is in practical units. We have introduced the critical density $n_{crit} \equiv (\varepsilon_0 m_e/e^2)\omega^2$, which is the usual definition for unmagnetised plasma. When discussing LPI, n_{crit} is for the pump wave ω_0. Significant Faraday rotation is thus possible in current ICF platforms with modest B fields. For instance, with $n_e/n_{crit} = 0.1$ and $B_{eq} = 10$ T, we obtain $\partial_z\phi = 16.8^\circ$/mm. This could be used to diagnose n_e (a common technique when feasible), and could affect LPI processes such as crossed-beam energy transfer.[29–31]

IV. IMPACT OF EXTERNAL B FIELD ON PARAMETRIC COUPLING

We apply the above theory to magnetized LPI in HED relevant conditions, all for $\vec{k}||\vec{B_{eq}}||\hat{z}$. We consider how the imposed field modifies stimulated Raman (SRS) and Brillouin (SBS) scattering, as well as stimulated whistler scattering (SWS) which only occurs in a background field. Recall $\vec{k}_i = k_i\hat{z}$ and we choose $k_0 > 0$. k_1 and k_2 can have either sign. Let c_i =sign(k_i) for $i = 1,2$. For all three parametric processes we discuss, "forward scatter" refers to the case where the scattered e/m wave propagates in the same direction as the pump ($c_1 = +1$), and "backward scatter" to the opposite case ($c_1 = -1$). To satisfy k matching, we cannot have both $c_1 = -1$ and $c_2 = -1$. For SRS and SBS, c_2 must equal +1, but for SWS $c_2 = -1$ is possible.

We do not consider growth rates, but focus instead on the "kinematics" of three-wave interactions, through the phase-matching conditions among free waves. We study the scattered e/m wave frequency ω_1, since this is what escapes the plasma and is measured experimentally. As discussed in section III C, $\vec{B_{eq}}$ causes the R and L waves to propagate with different phase velocities. Therefore, a laser or other external source that imposes a linearly-polarised light wave of frequency ω_0 couples to an R and an L wave in a magnetised plasma. For stimulated scattering, we are mostly interested in down-shifted scattered waves for which $\omega_1 < \omega_0$, which have the same polarisation as the pump: an R or L pump couples to a down-shifted R or L scattered wave, respectively, hence $\sigma_1 = \sigma_0$ which we sometimes denote as σ. We discuss SRS and SBS, which can be driven by either an R or L pump, and SWS, which can only be driven by an R pump (since the whistler wave is an R wave). Table III summarizes the processes we study.

In order to derive a dispersion relation for ω_1 in terms of known inputs, we begin with the identity $k_2 = k_2$. We use k matching to write $k_2 = k_0 - k_1$ on the left side, and the plasma-wave dispersion relation of interest to re-write the right side in terms of ω_2. We then use the e/m dispersion relation to write k_1 in terms of ω_1, and use ω matching to write $\omega_2 = \omega_0 - \omega_1$. For SRS and SWS this yields $k_0 - k_1 = (\omega_2^2 - \omega_{pe}^2)^{1/2}/v_{Te}3^{1/2}$. The same method is applied for SBS, where k_2 is written in terms of ω_2 using the simple IAW dispersion relation, $\omega_2 = c_s|k_2|$, for an approximate analysis (the numerical roots use the full e/s dispersion relation). That is, $c_s^2 = (Z_iT_e/m_i)(1 + 3T_i/Z_iT_e)$. The resulting dispersion relations can be summarised as follows:

$$\begin{aligned} &M_Y \equiv (1 - \Omega_{pe}^2(1 - \sigma_0\Omega_{ce})^{-1})^{1/2} \\ &- c_1\Omega_1(1 - \Omega_1^{-2}\Omega_{pe}^2(1 - \sigma_1\Omega_{ce}/\Omega_1)^{-1})^{1/2} - P_Y = 0 \end{aligned} \tag{92}$$

where Y is either RW, for SRS and SWS, or B, for SBS. For SRS and SWS $P_Y = P_{RW} = c_2V_e^{-1}((1-\Omega_1)^2 - \Omega_{pe}^2)^{1/2}$, where $V_e \equiv v_{Te}3^{1/2}/c$. For SBS, $P_Y = P_B = V_s^{-1}(1-\Omega_1)$, with $V_s \equiv c_s/c$. This is usually very small, with 10^{-3} a typical magnitude. $\Omega_X \equiv \omega_X/\omega_0$, where X denotes any angular frequency subscript in equation 92. The frequency of scattered light which satisfies phase matching is given by the roots of equation 92, which can be found by plotting M_Y vs. Ω_1. This is illustrated for SRS and SWS in figure 3, and for SBS in figure 4, for the parameters given in table I and $n_e/n_{crit} = 0.15$.

The dispersion relations given in equation 92 are plotted as a function of ω_1/ω_0 and n_e/n_{crit} for scattering geometries $(c_1, c_2) = (-1,1), (1,1), (1,-1)$, in figures 5, 6 and 7, respectively. The two dispersion relations, M_{RW} and M_B have been overplotted. To distinguish between them, M_{RW} has been cross-hatched, whilst M_B has not. The colour scale for M applies to both M_{RW} and M_B. The regions of figures 5, 6 and 7 where M is not real are coloured gray. The regions of the plot where $M_{RW,B} \neq 0$ serve only to illustrate the root-finding method employed: to ensure we have correctly identified roots, we check that $M_{RW,B}$ has changed sign. The roots of M have been computed numerically and are plotted as black contours. These contours indicate whether SRS, SBS or SWS can occur for the geometry and plasma conditions considered,

Process	pump e/m wave	scattered e/m wave	plasma wave	geometries (c_1, c_2)	ω_1 range	n_e/n_{crit} range
SRS	R,L	R,L	EPW	(1,1), (-1, 1)	$> \omega_{pe}$	$< 1/4$
SBS	R,L	R,L	IAW	(1,1), (-1, 1)	$\gtrsim \omega_0 - \omega_{pi}$	< 1
SWS	R	R-whistler	EPW	(1,-1), (-1, 1)	$< \omega_{ce}$	$\gtrsim (1 - \omega_{ce}/\omega_0)^2$ for $T_e = 0$

TABLE III: Summary of parametric processes we study. L, R refer to left, right polarised e/m waves.

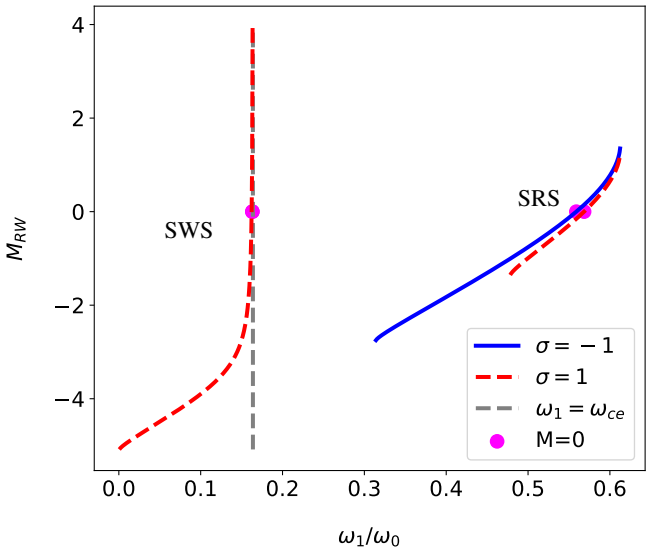


FIG. 3: The dispersion relation for SRS and SWS, M_{RW} is plotted vs. ω_1/ω_0. Its roots $M_{RW} = 0$ are indicted by magenta points. This is for backscatter ($c_1 = -1, c_2 = 1$) and the parameters of Table 1 plus $n_e/n_{crit} = 0.15$. SWS is possible for a right polarised pump (red), but cannot occur when the pump is left polarised (blue).

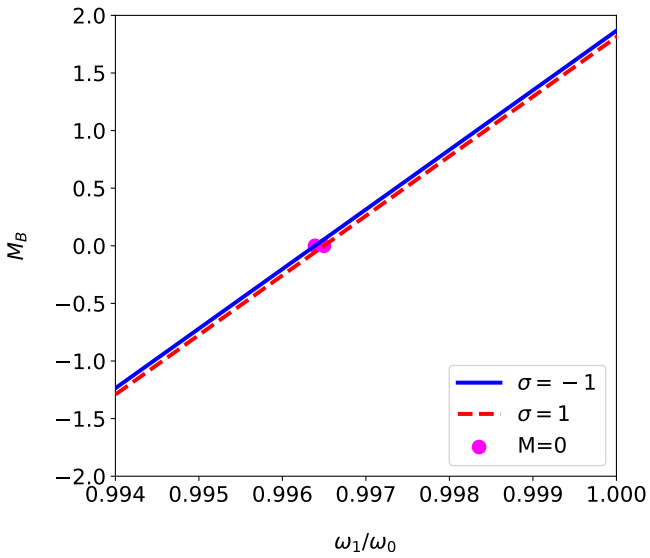


FIG. 4: The dispersion relation for SBS, M_B is plotted vs. ω_1/ω_0, for the same parameters as Fig. 3. Its roots $M_B = 0$ are indicted by magenta points. The roots of M_B occur at similar, but not identical ω_1/ω_0 for a left and right polarised pump.

and illustrate the relationship between the normalised plasma density and scattered EMW frequency for each of these processes. The contours which correspond to a given parametric process are appropriately labelled.

In figures 5 and 6 a sharp decrease can be seen in the frequency of SRS scattered light with increasing plasma density. Also in figures 5 and 7, the frequency of SWS scattered light rises with electron density before reaching a maximum, and falling. It is often useful to obtain limits in parameter space beyond which phase matching cannot occur. For example, in an unmagnetised plasma, SRS is only possible for $n_e/n_{crit} < 0.25$. The region of parameter space in which SWS can occur is also restricted, as $\omega_1 \leq \omega_{ce}$. Using the same method as for SRS, the following inequality is obtained for the normalised electron densities at which SWS can occur in a cold plasma:

$$\frac{n_e}{n_{crit}} \geq (1 - \omega_{ce}/\omega_0)^2 \tag{93}$$

These three limits are shown in figures 5, 6 and 7 in cyan, magenta and purple, respectively. Note that the contours for SRS and SWS always lie within $n_e/n_{crit} < 0.25$ and $\omega_1 \leq \omega_{ce}$ respectively, as expected. SWS does *not* respect Eq. 93, as discussed further below.

A. Stimulated Raman Scattering: SRS

The dispersion relation for SRS is given by equation 92, where $c_2 = 1$. For a cold plasma with $V_e = 0$, we find $\Omega_2 = \Omega_p$ always, so $\Omega_1 = 1 - \Omega_p$. This is true with or without a background field B_{eq}. Thus, any effect of B_{eq} on Ω_1 is "doubly small", in that it also relies on thermal effects. For no background field $\Omega_{ce} = 0$, we obtain the usual solutions, which for $V_e \ll 1$ and $\Omega_p \ll 1$ are $\Omega_1 \approx 1 - \Omega_p - (\Omega_p/2)V_e^2$ for $c_1 = 1$ (forward scatter), and $\Omega_1 \approx 1 - \Omega_p - (2/\Omega_p)V_e^2$ for $c_1 = -1$ (backscatter).

Including a weak background field, we write $\Omega_1 \approx \Omega_{1U} + \delta\Omega_1$ where Ω_{1U} is the solution for $\Omega_{ce} = 0$: $M[\Omega_{1U}, \Omega_{ce} = 0] = 0$. We have $M[\Omega_{1U} + \delta\Omega_1, \Omega_{ce}] \approx M[\Omega_{1U}, 0] + \delta\Omega_1(\partial M/\partial\Omega_1) + \Omega_{ce}\partial M/\partial\Omega_{ce} = 0$, which gives $\delta\Omega_1 \approx \alpha\Omega_{ce}$ with $\alpha = -(\partial M/\partial\Omega_{ce})/(\partial M/\partial\Omega_1)$. All partials are evaluated at $\Omega_1 = \Omega_{1U}$ and $\Omega_{ce} = 0$. One can find a formula for α, but it is unilluminating. We quote the result in the limit that $V_e \ll 1$ and $\Omega_p \ll 1$:

$$\alpha \approx c_1 \left(2/\Omega_p^2 + 1/\Omega_p + 2\right)^{\frac{1-c_1}{2}} \sigma_0 V_e^2 \Omega_p^3 \tag{94}$$

The full numerical solution of M_{RW} (see equation 92) is plotted in figures 8 and 9 for the plasma conditions given in table I and the first row of table II. The frequencies, wave vectors and, if applicable, the polarisations of the e/m and e/s waves

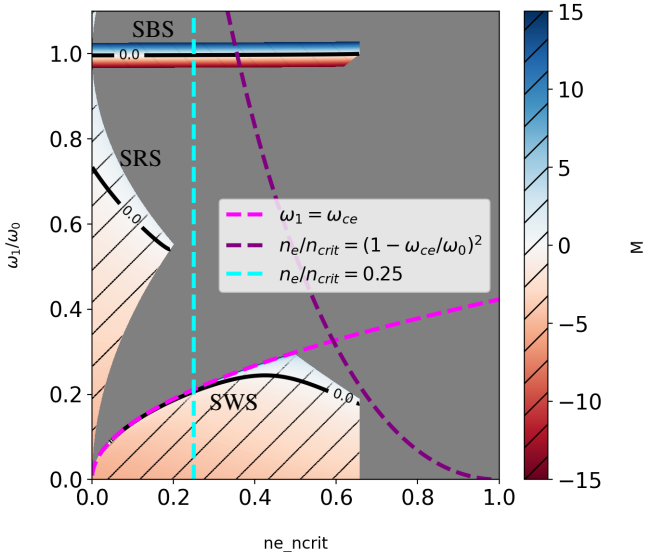


FIG. 5: The dispersion relations for SWS and SRS (M_{RW}) and SBS (M_B) vs. electron density and scattered light frequency. $T_e = 4$ keV, $T_i = 2$ keV, $\omega_{ce}/\omega_{pe} = 0.423$, and we consider backscatter ($c_1 = -1, c_2 = 1$). M_{RW} is distinguished by cross-hatching. The roots of M are plotted as black contours which have been labelled appropriately. Three other curves have been plotted: $n_e/n_{crit} = 0.25$, the maximum density at which SRS occurs, $\omega_1 = \omega_{ce}$, the maximum SWS frequency, and $n_e/n_{crit} \geq (1-\omega_{ce}/\omega_0)^2$, the *minimum* density at which SWS can occur in a cold plasma. Note that M_{RW} adheres to only the first two of these approximate analytic limits.

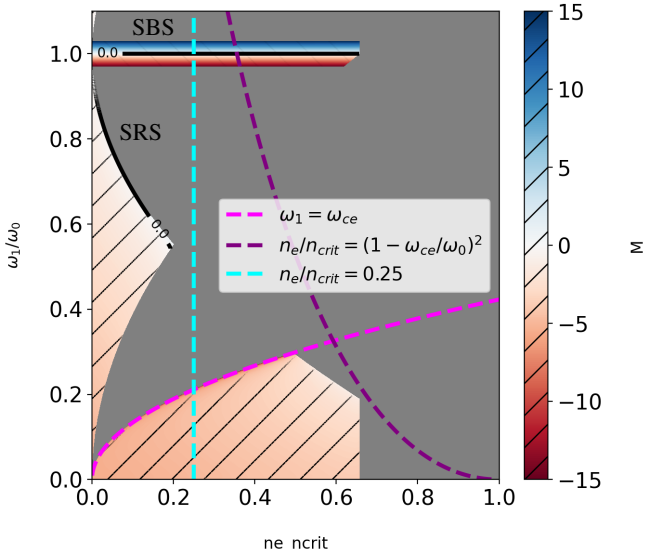


FIG. 6: As figure 5, but for forward scatter ($c_1 = c_2 = 1$). Only SRS can occur for this geometry. While SBS is kinematically possible, the ion wave has $k_2, \omega_2 = 0$, and SBS has 0 growth rate. Thus, the solution plotted is spurious. For this geometry, SWS is kinematically disallowed.

at which phase-matching conditions are met are illustrated by parallelograms. Specifically, figures 8 and 9 correspond to

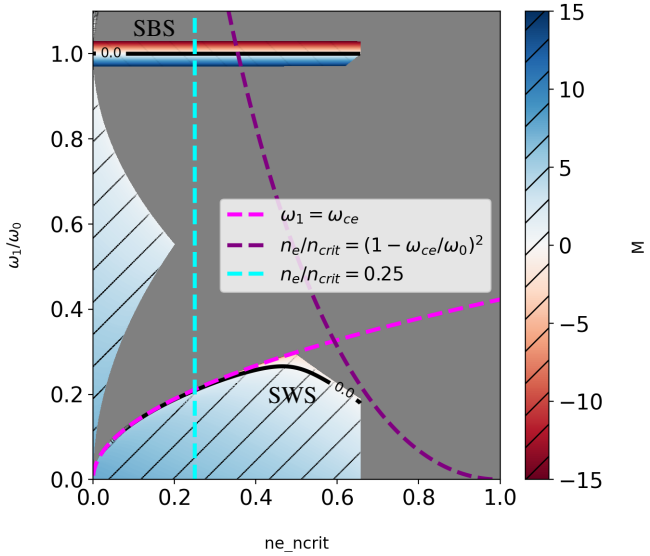


FIG. 7: As figure 5, but for $c_1 = 1$ and $c_2 = -1$. For this geometry, phase matching is only satisfied for SWS, and unphysical SBS as in figure 6. As in figure 5, $M_{RW} = 0$ is only satisfied for densities above the minimum normalised electron density in a cold plasma, $n_e/n_{crit} \geq (1-\omega_{ce}/\omega_0)^2$, which is plotted in purple.

forward and back-SRS, respectively.

The shift in wavelength of SRS light due to the presence of the external magnetic field, $\Delta\lambda_1 = \lambda_1 - \lambda_1(\omega_{ce} = 0)$, is given by

$$\frac{\Delta\lambda_1}{\lambda_0} = \omega_0 \left(\frac{1}{\omega_1} - \frac{1}{\omega_1(\omega_{ce} = 0)} \right) \tag{95}$$

Substituting from equation 85, and treating temperature and magnetic field as small perturbations in Ω_1 as detailed above, we derive the following expression for $\Delta\lambda_1$ to first order in Ω_{ce} and Ω_{pe}^2:

$$\frac{\Delta\lambda_1}{\lambda_0} \approx -\frac{\delta\Omega_1}{\Omega_{1U}^2} \tag{96}$$

or equivalently

$$\Delta\lambda_1[nm] \approx -c_1\lambda_0^2[\mu m^2]\frac{5.48\times10^{-4}}{\Omega_{1U}^2}Te[keV]\left(\frac{n_e}{n_{crit}}\right)^{3/2} B[T]\left(2\frac{n_{crit}}{n_e} + \sqrt{\frac{n_{crit}}{n_e}} + 2\right)^{\frac{1-c_1}{2}}\sigma_0 \tag{97}$$

in practical units. Under the conditions given in table I, for $n_e/n_{crit} = 0.15$ and $B = 100$T for SRS backscattered light from a left-polarised pump wave, the analytic approximation yields $\Delta\lambda_1 = -0.041$nm, compared to the full numerical solution, which gives $\Delta\lambda_1 = -0.046$nm. Typically, in NIF-type experiments, the wavelength of back-SRS light is in the range 500-600nm, with a spectral width of 5-10nm due to damping and gradients. Given that this is the case, detecting sub-Angstrom shifts in this spectrum presents a significant challenge. This first-order approximation of $\Delta\lambda_1$ agrees

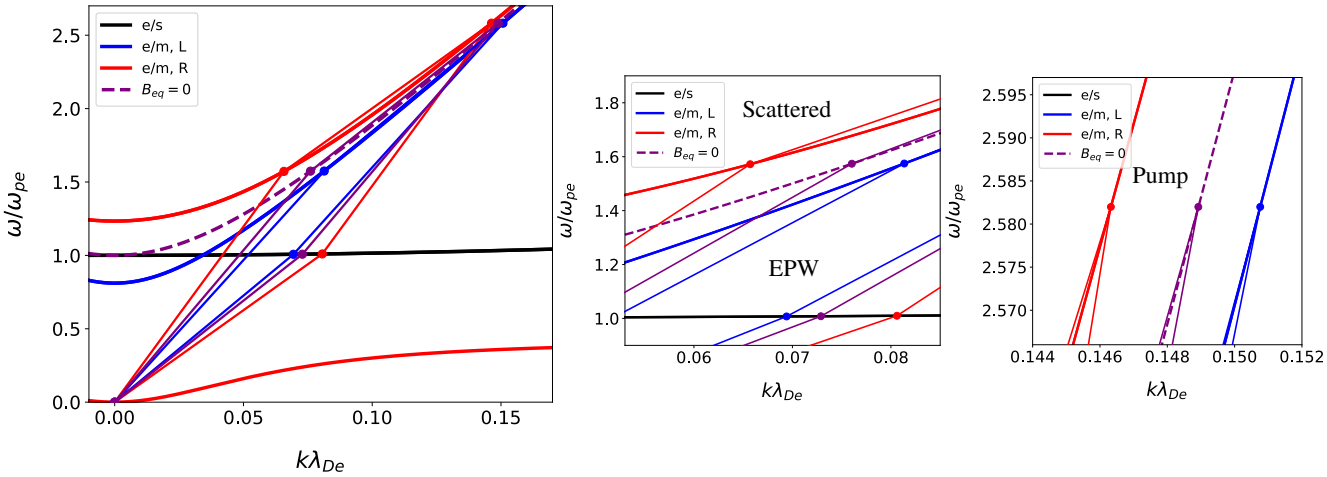


FIG. 8: Phase-matching parallelograms for forward-SRS light for plasma conditions given in table I, with $n_e/n_{crit} = 0.15$. The right and left-polarised e/m waves are plotted in red and blue, respectively, while the unmagnetised e/m wave and the electrostatic EPW are shown in purple and black, respectively. The phase-matching parallelograms are colour-coded according to the polarisation of the pump wave. The pump frequency ω_0 is fixed in all cases, which gives slightly different k_0's from the relevant dispersion relations. The scattered e/m frequencies ω_1 are *nearly* but not exactly the same, though this is very hard to see visually. The pump and scattered e/m waves have the same handedness.

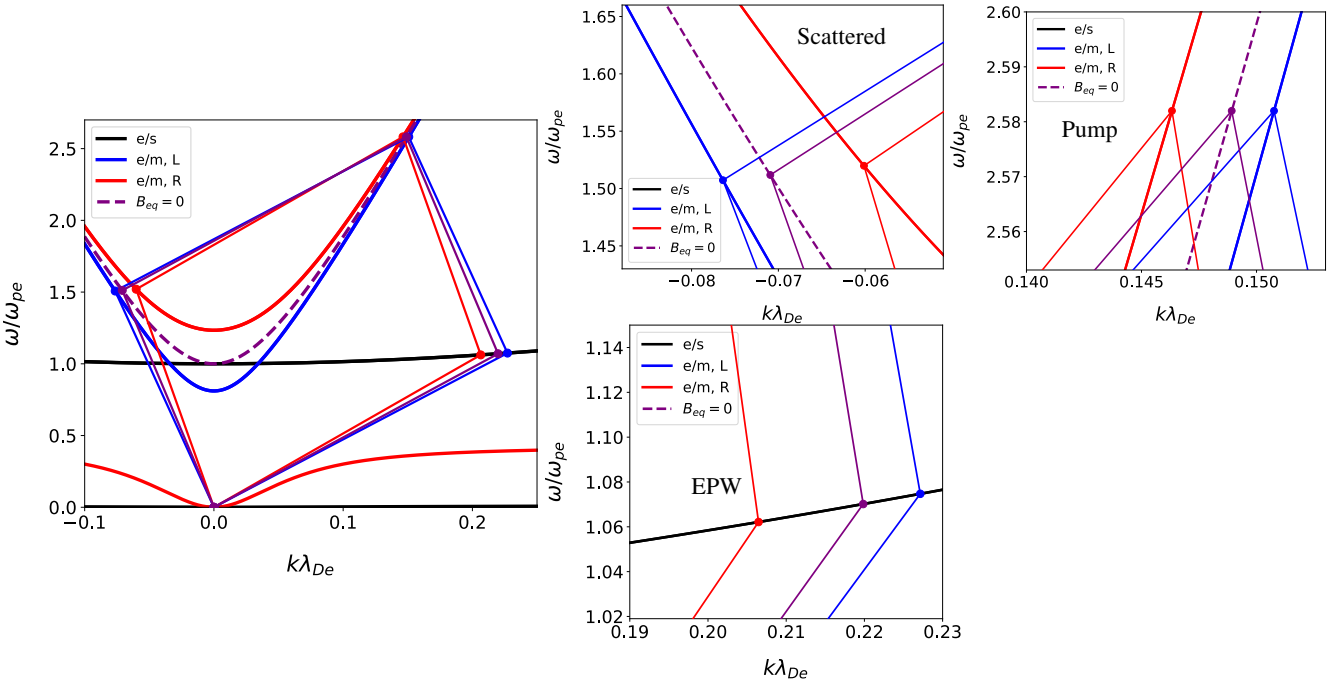
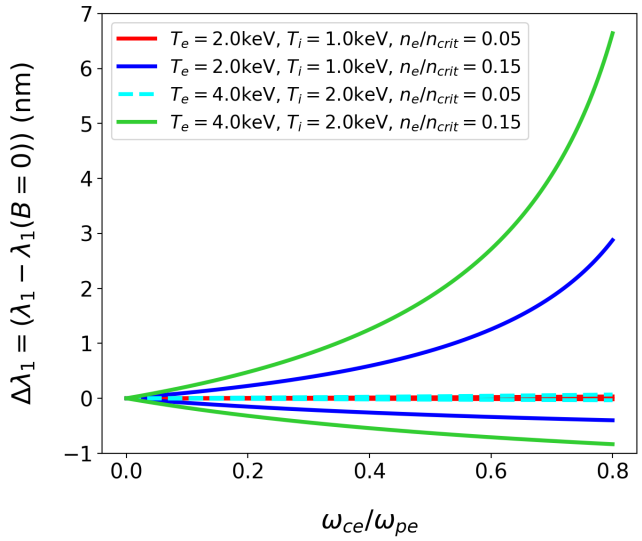


FIG. 9: Phase-matching parallelograms for backward-SRS light: otherwise same as Fig. 8.

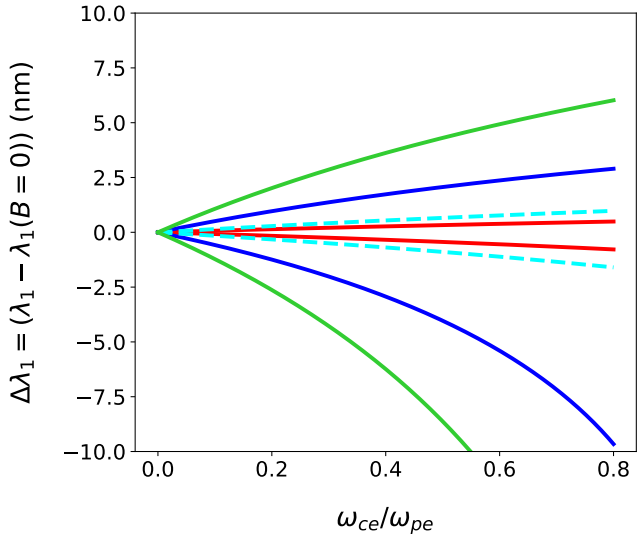
reasonably closely with the full numerical computation of $\Delta\lambda_1$,which is plotted as a function of ω_{ce}/ω_{pe} for $T_e = 2$keV, 4keV and $n_e/n_{crit} = 0.05$, 0.15 in figures 10a and 10b, for forward and back-SRS light, respectively. The effect of electron density and temperature become particularly significant for forward and backward-SRS light from a right-polarised pump as $\omega_{ce} \to \omega_{pe}$, as in this limit, $\Delta\lambda_1 \to \infty, -\infty$, respectively.

B. Stimulated Brillouin Scattering: SBS

The phase matching relation for SBS, $M_B = 0$ is derived in section IV, and given in equation 92. Exact forward SBS ($c_1 = 1$) is not considered since in our strictly 1D geometry it does not occur. $M_B = 0$ has a spurious root for $k_2 = \omega_2 = 0$, which connects to near-forward scatter for small but nonzero angle between $\vec{k}_0$ and $\vec{k}_1$. The SBS growth rate is zero for $k_2 = 0$, so we discuss only backscatter ($c_1 = -1$, $c_2 = 1$). For

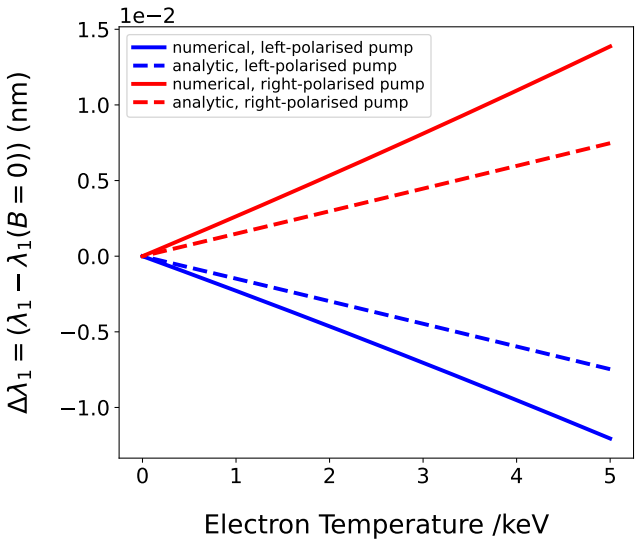


(a)

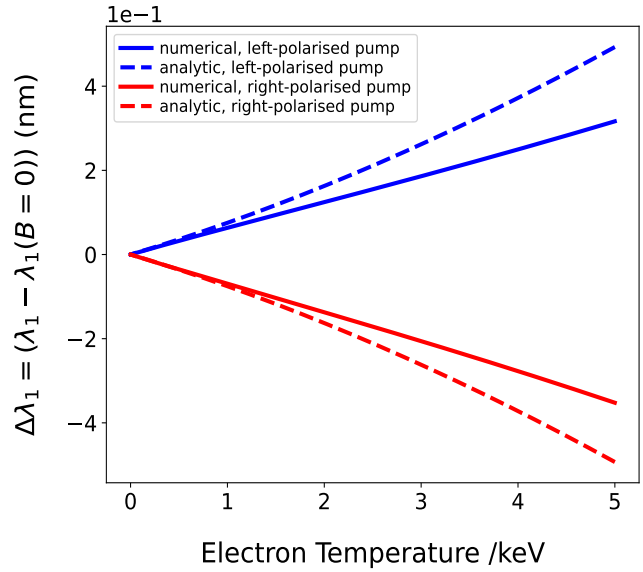


(b)

FIG. 10: $\Delta\lambda_1$, the difference in wavelength of forward (10a) and backward (10b) SRS light in a magnetised versus an unmagnetised plasma, for $T_e = 2.0$keV, 4.0keV, $n_e/n_{crit} = 0.05$, 0.15 and $\lambda_0 = 351$nm. For [forward, backward] SRS, $\Delta\lambda_1$ is $[>0, <0]$ for a right-polarised pump and $[<0, >0]$ for a left-polarised pump.



(a)



(b)

FIG. 11: $\Delta\lambda_1$ of forward (11a) and backward (11b) SRS light, plotted for $\omega_{ce}/\omega_{pe} = 0.1$, $\frac{n_e}{n_{crit}} = 0.05$ and $\lambda_0 = 351$nm. Full numerical solutions are unbroken lines, first-order analytic approximations are dashed lines.

$\Omega_{ce} = 0$, the exact solution is

$$\Omega_{1U} = \frac{1 - 2\eta_0 V_s + V_s^2}{1 - V_s^2} \approx 1 - 2\eta_0 V_s \tag{98}$$

with $\eta_0 \equiv (1 - \Omega_{pe}^2)^{1/2}$. The approximate form for $V_s \ll 1$ is typically quite accurate. The correction for a weak B field and to leading order in V_s^2 is

$$\delta\Omega_1 = \sigma_0 \Omega_{pe}^2 V_s \Omega_{ce} (1 + V_s) \tag{99}$$

For simplicity, we set the final factor to 1 below. As with SRS, the correction is "doubly small" since it scales with the product of $V_s \propto T_e^{1/2}$ and Ω_{ce}. The scattered wavelength shift $\delta\lambda_1 \equiv \lambda_1 - \lambda_1[\Omega_{ce} = 0]$, evaluated at $\Omega_{1U} = 1$, is

$$\frac{\delta\lambda_1}{\lambda_0} \approx -\sigma_0 \Omega_{pe}^2 V_s \Omega_{ce} (1 + V_s) \tag{100}$$

In practical units,

$$\delta\lambda_1[Ang.] \approx -9.67 \times 10^{-4} \sigma_0 \frac{n_e}{n_{crit}} B[T] \sqrt{\frac{Z_i T_e[keV]}{A_i}\left(1 + \frac{3T_i[keV]}{Z_i T_e[keV]}\right)} \lambda_0^2[\mu m^2] \tag{101}$$

This is an extremely small value for ICF conditions. For the parameters shown in table II, with $\lambda_0 = 351$ nm, $n_e/n_{crit} =$

0.15, $B = 100$T and a right-polarised pump, the analytic approximation gives $\delta\lambda_1 \approx -2.37$pm, whereas the full numerical solution gives $\delta\lambda_1 \approx -2.41$pm.

C. Stimulated Whistler Scattering: SWS

We now discuss SWS, which only occurs with a background magnetic field. It resembles SRS, except the scattered e/m wave is a low-frequency whistler ($\omega_1 < \omega_{ce}$). For a cold plasma, this imposes a *minimum* density of $n_e/n_{crit} \geq (1-\omega_{ce}/\omega_0)^2$ to satisfy frequency matching, as opposed to a *maximum* of $n_e/n_{crit} < 1/4$ for SRS. Forward ($c_1 = +1, c_2 = -1$) and backward ($c_1 = -1, c_2 = +1$) SWS are both kinematically allowed, though forward SWS can only occur for a plasma wave propagating counter to the pump: $c_2 = -1$. The phase-matching condition M_{RW} for SWS, given in equation 92, is identical to that of SRS except that $c_2 = \pm 1$. Figures 17 and 15 show SWS phase matching diagrams for the allowed geometries and for a range of n_e/n_{crit}, ω_{ce}/ω_{pe} and T_e.

The relationship between ω_1/ω_0, $k_2\lambda_{De}$ and ω_{ce}/ω_{pe} is shown in figures 18 and 16 for $(c_1, c_2) = (-1, 1), (1, -1)$, respectively, for a range of plasma densities and temperatures. The frequency of the scattered EMW increases with increasing magnetic field strength, before saturating. The rate of increase with ω_{ce}/ω_{pe}, and the values of ω_1/ω_0 and ω_{ce}/ω_{pe} at which saturation occurs vary with plasma density and temperature. Increasing T_e decreases the ω_1/ω_0 at which the trend saturates, while increasing n_e/n_{crit} causes the observed trend to saturate at lower ω_1/ω_0 and ω_{ce}/ω_{pe}. $k_2\lambda_{De}$ is plotted to indicate the magnitude of Landau damping, which is expected to significantly reduce SWS growth for $k_2\lambda_{De} \gtrsim 0.5$. In the opposite limit, the SWS growth rate approaches zero as $k_2\lambda_{De} \to 0$.

The wavelength of SWS scattered light is

$$\lambda_1[\mu m] = \frac{\omega_{ce}}{\omega_1}\frac{10709.7}{B[T]} \tag{102}$$

For the bottom rows of table IV, $n_e/n_{crit} = 0.15$, $\omega_{ce}/\omega_{pe} = 0.423$, and $\omega_1 \approx \omega_{ce}$. For a pump wavelength of $0.351\mu m$, we have $B = 5000$T and $\lambda_1 \approx 2.14\mu$m. This is in the near infrared, where detectors exist but are not commonly fielded on ICF lasers. More realistic B fields will be much lower, and λ_1 much longer.

In order for SWS scattered light to be detected, it must first leave the plasma and propagate to a detector. Given the long wavelength of SWS scattered light, there is a possibility that changing plasma conditions experienced by the wave as it propagates through the plasma may cause it to become evanescent. Consider equation 77. Rearranging for k, we obtain:

$$c^2k^2 = \omega^2 - \frac{\omega_{pe}^2}{1-\sigma\frac{\omega_{ce}}{\omega}} \tag{103}$$

We see that for $\omega^2 > \frac{\omega_{pe}^2}{1-\sigma\frac{\omega_{ce}}{\omega}}$, k is real and the wave can propagate. If the reverse is true, k is imaginary and the wave is evanescent. ω_{pe} and ω_{ce} vary in space, and generally go to zero far from the target. If B tends to zero too rapidly, the dispersion relation tends to the unmagnetised one, $c^2k^2 = \omega^2 - \omega_{pe}^2$. In this case, if n_e exceeds the critical density of the SWS scattered light wave, the wave will be reflected and will not reach the detector. However, if the magnetic field strength decreases slowly enough and/or the electron density decreases quickly enough, the wave will escape the plasma. Then $\omega_{pe} = 0$ and $ck = \omega$, that is, it becomes a vacuum light wave and can propagate to the detector.

We now discuss the variation of SWS with plasma parameters. For finite T_e, Langmuir-wave frequency increases, an effect comparable to an increase in electron density. This enables SWS to occur at densities lower than the minimum density in a cold plasma, given in eqn 93. We see this in Fig. 15, where the lowest density shown, $n_e/n_{crit} = 0.15$, corresponds to the highest pump frequency and a very high Langmuir-wave frequency, $\omega_2/\omega_{pe} > 2$. This requires a large $k_2\lambda_{De} > 1$, which entails considerable Landau damping and therefore a low SWS growth rate. Although growth rates are beyond the scope of this paper, other work establishes that they generally are $\propto k_2^p$ (for some power p) when $k_2\lambda_{De}$ is small, and decrease with increasing Landau damping for large $k_2\lambda_{De}$. This means there is an effective low-density cut-off, below which SWS is kinematically allowed but strongly damped. In the opposite limit, as n_e approaches n_{crit} (such as $n_e/n_{crit} = 0.6$ in figures 15 and 18 and table IV), k_2 becomes small and Landau damping is negligible, however the growth rate of SWS also tends to 0. There is thus an intermediate range of n_e in which the growth rate is optimal, and $k_2\lambda_{De}$ is moderate. The case where $n_e/n_{crit} = 0.4$ and $T_e = 2$ keV shown in the figures 15 and 17 and table IV typifies this regime.

c_1	c_2	n_e/n_{crit}	T_e [keV]	ω_1/ω_0	ω_1/ω_{ce}	$k_2\lambda_{De}$	$(1-\frac{\omega_{ce}}{\omega_0})^2$
-1	1	0.6	0.5	0.2212	0.6752	0.0592	0.452
1	-1	0.6	0.5	0.224	0.6836	0.0336	0.452
-1	1	0.6	4	0.1995	0.609	0.1502	0.452
1	-1	0.6	4	0.2163	0.6601	0.0883	0.452
-1	1	0.4	2	0.2557	0.9557	0.3582	0.5365
1	-1	0.4	2	0.2615	0.9776	0.3479	0.5365
-1	1	0.15	4	0.1623	0.9904	1.1074	0.6992
1	-1	0.15	4	0.1631	0.9955	1.106	0.6992

TABLE IV: Frequencies of stimulated whistler scattered light for several n_e/n_{crit} and T_e (ion temperature, $T_i = T_e/2$), and their corresponding values of the normalised EPW wavenumber. For all cases, $\omega_{ce}/\omega_{pe} = 0.423$. The rightmost column is the minimum n_e/n_{crit} for SWS to occur in a cold plasma.

V. CONCLUSION

We presented a warm-fluid theory for magnetized LPI, for the simple geometry of all wavevectors parallel to a uniform, background field. The field affects the electromagnetic linear waves in a plasma, though the electrostatic waves are unaffected for our geometry. Specifically, the right and left circular polarised e/m waves become non-degenerate, and form the natural basis, as opposed to linearly polarised waves. This

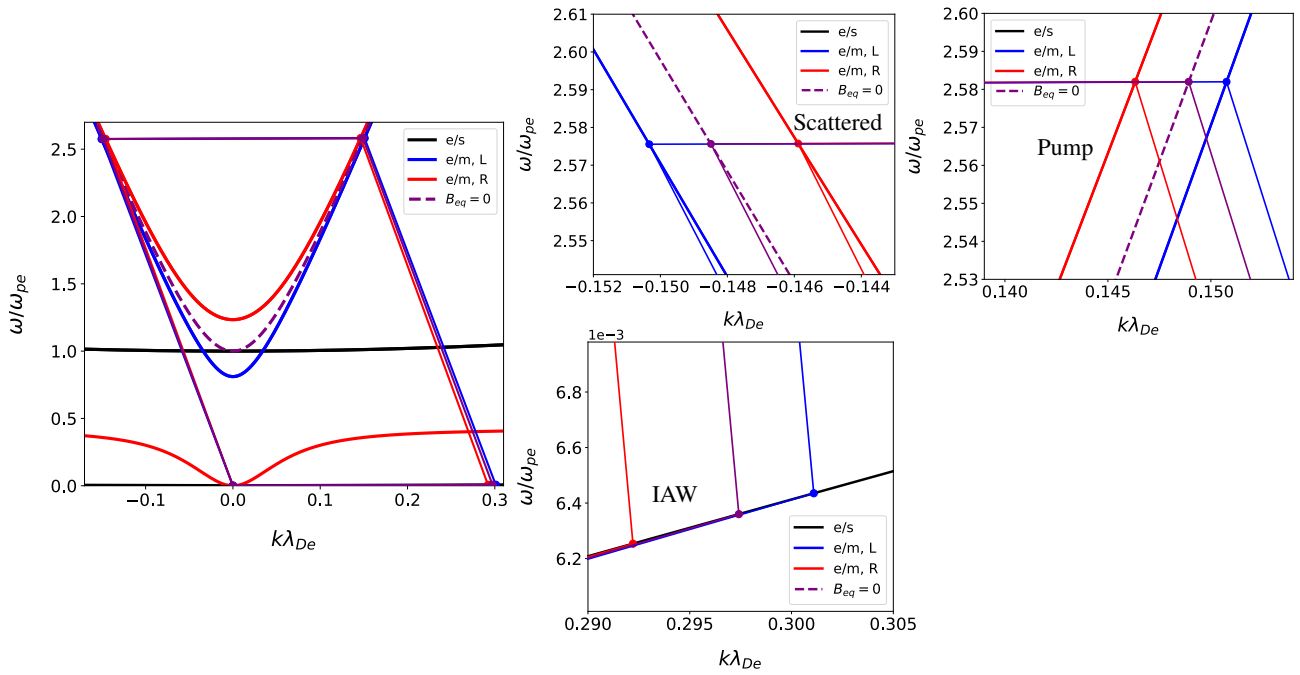


FIG. 12: Phase-matching parallelograms for backward-SBS, otherwise same as Fig.8. Electrostatic IAW shown in black.

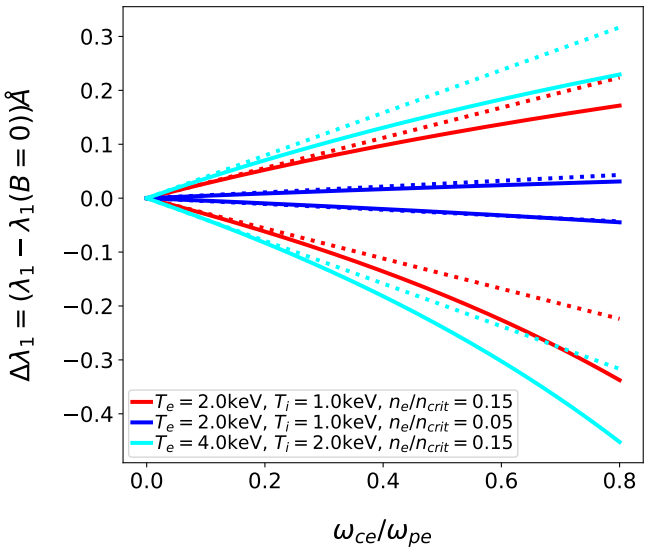


FIG. 13: $\delta\lambda_1$, the difference in wavelength of backward-SBS light in a magnetised versus an unmagnetised plasma, for three combinations of electron temperatures and densities $T_e = 2.0$keV, 4.0keV, and $n_e/n_{crit} = 0.05, 0.15$, where the ratio of electron and ion temperature is kept constant: $T_e/T_i = 2$. The laser wavelength, $\lambda_0 = 351$nm. The full numerical solutions and their analytic counterparts are plotted as unbroken and dashed lines, respectively. $\Delta\lambda_1[<0, >0]$ for a right or left-polarised pump, respectively.

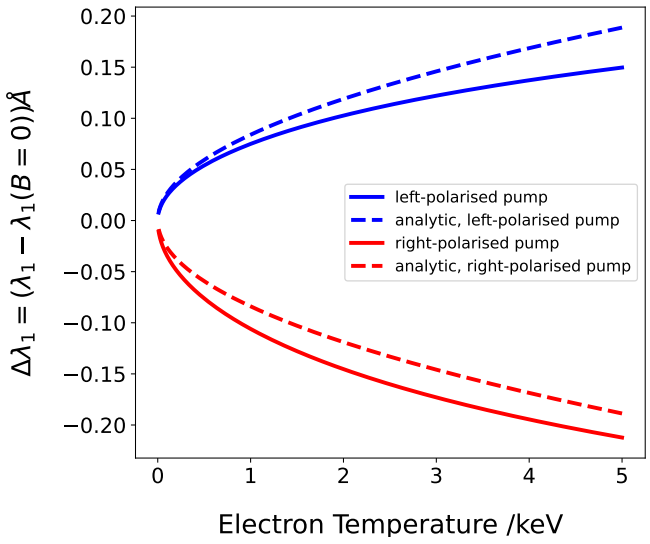


FIG. 14: $\Delta\lambda_1$ of backwards SBS light, plotted for $\omega_{ce}/\omega_{pe} = 0.423$, $\frac{n_e}{n_{crit}} = 0.15$ and $\lambda_0 = 351$nm. Full numerical solutions are unbroken lines, analytic approximations as dashed lines.

allows for Faraday rotation, which could be significant on existing ICF laser facilities for magnetic fields imposable with current technology. The field introduces two new e/m waves, the ion cyclotron and whistler wave, with no analogues in an unmagnetised plasma.

We found a parametric dispersion relation to first order in parametric coupling, Eq. 67, analogous to the classic 1974 work of Drake[24]. We then focused on the kinematics of phase matching for three-wave interactions. Since the right and left circular polarised light waves have different k vectors for the same frequency, the background field introduces a small shift in the scattered SRS and SBS frequencies compared to the unmagnetised case. The sign of the shift depends on the pump polarization and forward vs. backward scatter. The shift's

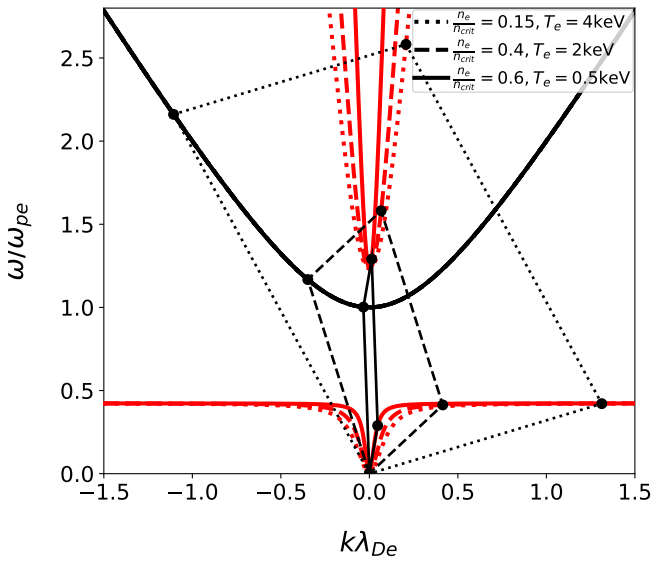


FIG. 15: Phase-matching parallelogram for forward SWS: $c_1 = 1, c_2 = -1$, where $\omega_{ce}/\omega_{pe} = 0.423$ and $T_i = T_e/2$.

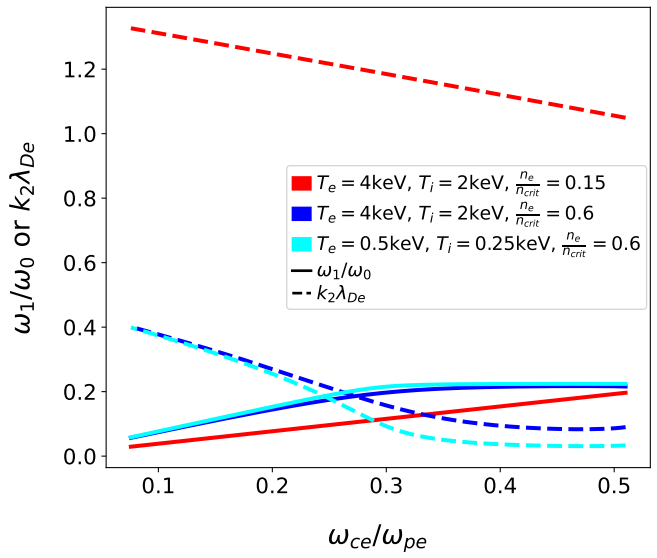


FIG. 16: Frequency (unbroken lines) of forward-SWS scattered light ($c_1 = 1, c_2 = -1$), and Langmuir wave $k_2\lambda_{De}$ (dashed lines) for various plasma densities, $n_e/n_{crit} = 0.6, 0.15$, and species temperatures, $T_e = 4, 0.5$keV, $T_i = T_e/2$keV. $k_2\lambda_{De}$ is plotted to indicate the strength of Landau damping.

magnitude increases with magnetic field, electron temperature, and plasma density. The wavelength shifts are $\lesssim 1$ Ang. for SRS, and $\lesssim 0.1$ Ang. for SBS, for plasma and magnetic field conditions currently accessible on lasers like NIF. Such small shifts would be extremely challenging to detect.

The new waves supported by the background B field also allow new parametric processes, such as stimulated whistler scattering (SWS) which we studied in detail. In this process, a light wave decays to a whistler wave and Langmuir wave. This is analogous to Raman scattering, with the whistler replacing the scattered light wave. We expect SWS scattered

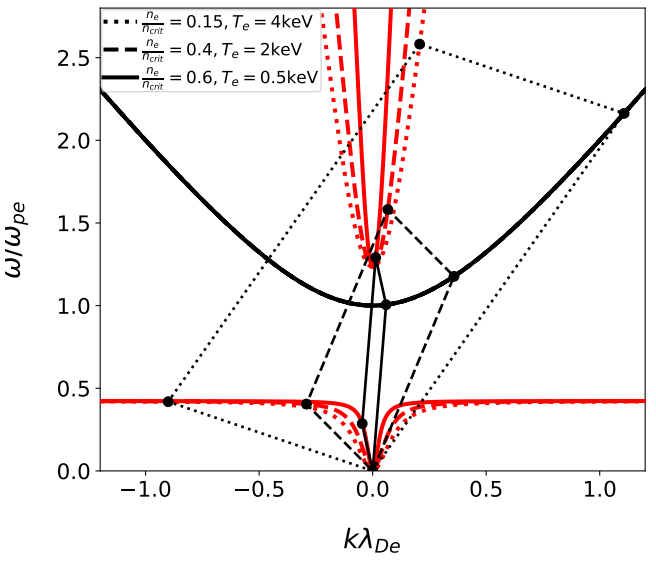


FIG. 17: Phase-matching parallelogram for backward SWS ($c_1 = -1, c_2 = 1$), for a range of electron densities and temperatures, where $\omega_{ce}/\omega_{pe} = 0.423$ and $T_i = T_e/2$.

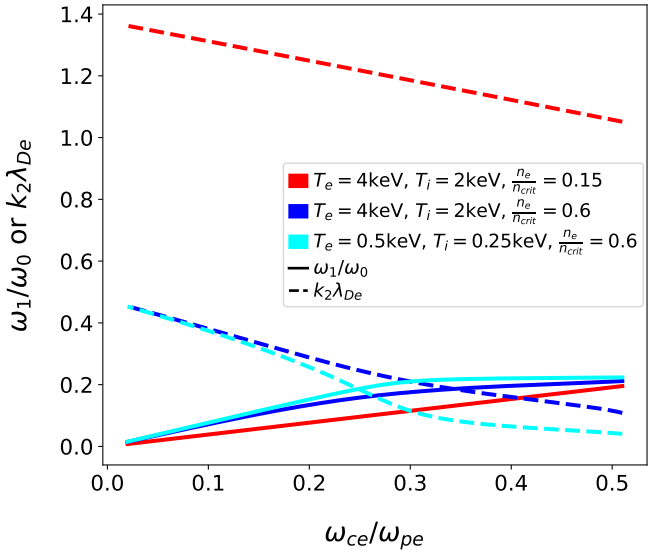


FIG. 18: Frequency backward SWS light with $c_2 = 1$, for $n_e/n_{crit} = 0.6, 0.15$ and $T_e = 4, 0.5$keV.

light to be infrared, with wavelength 1 to 100 μm for fields of 10 kT to 100 T. The whistler wavelength was found to decrease with increasing magnetic field strength, and increase with increasing plasma density and temperature. In a cold plasma ($T_e = 0$), there is a *minimum* density for SWS to satisfy phase matching, namely $n_e/n_{crit} > (1 - \omega_{ce}/\omega_0)^2$. Finite T_e allows us to circumvent this limit, at the price of high Langmuir-wave $k\lambda_{De}$ and thus strong Landau damping. We expect an analysis of SWS growth rates, including Landau damping, to show maximum growth for moderate $k\lambda_{De}$.

Much work remains to be done on magnetized LPI. This paper does not discuss parametric growth rates, though they are contained in our parametric dispersion relation (without damping or kinetics), and others have studied them in the

limit of weak coupling[18]. It is important to know when the two circularly-polarised light waves generated by a single linearly-polarised laser (incident from vacuum) should be treated as independent pumps, with half the intensity of (and thus lower growth rates than) the original laser. This likely occurs when the wavevector spread exceeds an effective bandwidth set by damping, inhomogeneity, or parametric coupling

Two major limitations to our model are the restriction to wavevectors parallel to the background field, and the lack of kinetic effects especially in the plasma waves. Propagation at an angle to the B field opens up many rich possibilities, including waves of mixed e/m and e/s character, and B field effects on the e/s waves. In the case of perpendicular propagation, the e/s waves become Bernstein waves. Adding kinetics is essential to understanding parametric growth in many systems of practical interest, where collisionless (Landau) damping is dominant. This also raises the so-called "Bernstein-Landau paradox", since Bernstein waves are naïvely undamped for any field strength.

If these issues can be resolved, we envisage magnetized LPI modelling tools analogous to existing ones for unmagnetised LPI. This was one of the main initial motivations for this work. For instance, linear kinetic coupling in the convective steady state and strong damping limit has been a workhorse in ICF for many years, such as for Raman and Brillouin backscatter[32] and crossed-beam energy transfer[31]. A magnetized generalization of this needs to handle propagation at arbitrary angles to the B field, as well as arbitrary field strength. Among other things, it must correctly recover the unmagnetised limit. A suitable linear, kinetic, magnetized dielectric function will be one of the key enablers.

It is a pleasure to thank Y. Shi and B. I. Cohen for many fruitful discussions. This work was performed under the auspices of the U.S. Department of Energy by Lawrence Livermore National Laboratory under Contract DE-AC52-07NA27344. This document was prepared as an account of work sponsored by an agency of the United States government. Neither the United States government nor Lawrence Livermore National Security, LLC, nor any of their employees makes any warranty, expressed or implied, or assumes any legal liability or responsibility for the accuracy, completeness, or usefulness of any information, apparatus, product, or process disclosed, or represents that its use would not infringe privately owned rights. Reference herein to any specific commercial product, process, or service by trade name, trademark, manufacturer, or otherwise does not necessarily constitute or imply its endorsement, recommendation, or favoring by the United States government or Lawrence Livermore National Security, LLC. The views and opinions of authors expressed herein do not necessarily state or reflect those of the United States government or Lawrence Livermore National Security, LLC, and shall not be used for advertising or product endorsement purposes.

[1]G. E. Kemp, J. D. Colvin, B. E. Blue, and K. B. Fournier, "Simulation study of enhancing laser driven multi-kev line-radiation through application of external magnetic fields," Physics of Plasmas **23**, 101204 (2016), https://doi.org/10.1063/1.4965236.

[2]D. B. Schaeffer, W. Fox, D. Haberberger, G. Fiksel, A. Bhattacharjee, D. H. Barnak, S. X. Hu, and K. Germaschewski, "Generation and evolution of high-mach-number laser-driven magnetized collisionless shocks in the laboratory," Phys. Rev. Lett. **119**, 025001 (2017).

[3]S. A. Slutz, M. C. Herrmann, R. A. Vesey, A. B. Sefkow, D. B. Sinars, D. C. Rovang, K. J. Peterson, and M. E. Cuneo, "Pulsed-power-driven cylindrical liner implosions of laser preheated fuel magnetized with an axial field," Physics of Plasmas **17**, 056303 (2010), https://doi.org/10.1063/1.3333505.

[4]M. R. Gomez, S. A. Slutz, A. B. Sefkow, D. B. Sinars, K. D. Hahn, S. B. Hansen, E. C. Harding, P. F. Knapp, P. F. Schmit, C. A. Jennings, T. J. Awe, M. Geissel, D. C. Rovang, G. A. Chandler, G. W. Cooper, M. E. Cuneo, A. J. Harvey-Thompson, M. C. Herrmann, M. H. Hess, O. Johns, D. C. Lamppa, M. R. Martin, R. D. McBride, K. J. Peterson, J. L. Porter, G. K. Robertson, G. A. Rochau, C. L. Ruiz, M. E. Savage, I. C. Smith, W. A. Stygar, and R. A. Vesey, "Experimental demonstration of fusion-relevant conditions in magnetized liner inertial fusion," Phys. Rev. Lett. **113**, 155003 (2014).

[5]R. Jones and W. Mead, "The physics of burn in magnetized deuterium-tritium plasmas: spherical geometry," Nuclear Fusion **26**, 127–137 (1986).

[6]I. Lindemuth and R. Kirkpatrick, "Parameter space for magnetized fuel targets in inertial confinement fusion," Nuclear Fusion **23**, 263–284 (1983).

[7]W. L. Kruer, *The Physics of Laser Plasma Interactions* (Westview Press, Boulder, CO, 2003).

[8]J. D. Lindl, P. Amendt, R. L. Berger, S. G. Glendinning, S. H. Glenzer, S. W. Haan, R. L. Kauffman, O. L. Landen, and L. J. Suter, "The physics basis for ignition using indirect-drive targets on the national ignition facility," Physics of Plasmas **11**, 339–491 (2004), https://doi.org/10.1063/1.1578638.

[9]G. Velarde, Y. Ronen, and J. M. Martinez-Val, *Nuclear Fusion by Inertial Confinement: A Comprehensive Treatise* (CRC press, 1993) pp. 360, 361.

[10]R. K. Kirkwood, D. J. Strozzi, P. A. Michel, D. A. Callahan, B. Raymond, G. Gururangan, B. J. MacGowan, and N. Team, "Laser backscatter damage risk assessments of nif target experiments," in *APS Division of Plasma Physics Meeting Abstracts*, APS Meeting Abstracts, Vol. 2014 (2014) p. NP8.117.

[11]T. Chapman, P. Michel, J.-M. G. Di Nicola, R. L. Berger, P. K. Whitman, J. D. Moody, K. R. Manes, M. L. Spaeth, M. A. Belyaev, C. A. Thomas, and B. J. MacGowan, "Investigation and modeling of optics damage in high-power laser systems caused by light backscattered in plasma at the target," Journal of Applied Physics **125**, 033101 (2019), https://doi.org/10.1063/1.5070066.

[12]J. D. Lindl, *Inertial Confinement Fusion: The Quest for Ignition and Energy Gain Using Indirect Drive* (Springer-Verlag, 1998) Chap. 11.

[13]L. J. Perkins, B. G. Logan, G. B. Zimmerman, and C. J. Werner, "Two-dimensional simulations of thermonuclear burn in ignition-scale inertial confinement fusion targets under compressed axial magnetic fields," Physics of Plasmas **20**, 072708 (2013), https://doi.org/10.1063/1.4816813.

[14]L. J. Perkins, D. J. Strozzi, M. A. Rhodes, B. G. Logan, D. D. Ho, and S. A. Hawkins, "The application of imposed magnetic fields to ignition and thermonuclear burn on the national ignition facility," Bulletin of the American Physical Society **59** (2014).

[15]J. Moody, B. Pollock, H. Sio, D. Strozzi, D. Ho, C. Walsh, S. Kucheyev, B. Kozioziemski, E. Carroll, J. Fry, *et al.*, "Progress on the magnetized ignition experimental platform for the national ignition facility," APS (APS, 2021).

[16]N. M. Laham, A. S. A. Nasser, and A. M. Khateeb, "Effects of Axial Magnetic Fields on Backward Raman Scattering in Inhomogeneous Plasmas," Physica Scripta **57**, 253–257 (1998).

[17]L. STENFLO and G. BRODIN, "On the parametric decay of a circularly polarized wave," Journal of Plasma Physics **77**, 431–435 (2011).

[18]Y. Shi, "Three-wave interactions in magnetized warm-fluid plasmas: General theory with evaluable coupling coefficient," Phys. Rev. E **99**, 063212 (2019).

[19]B. J. Winjum, F. S. Tsung, and W. B. Mori, "Mitigation of stimulated raman scattering in the kinetic regime by external magnetic fields," Phys. Rev. E **98**, 043208 (2018).

[20]D. W. Forslund, J. M. Kindel, and E. L. Lindman, "Parametric excitation of electromagnetic waves," Phys. Rev. Lett. **29**, 249–252 (1972).

[21]L. Stenflo and G. Brodin, "Parametric decay of whistler waves in electron magnetohydrodynamics," **83**, 069801 (2010).

[22]A. Kumar and V. K. Tripathi, "Stimulated scattering of a whistler off an ion bernstein wave," Physica Scripta (Online) **84**, 5 (2011).

[23]M. Porkolab and R. P. H. Chang, "Nonlinear wave effects in laboratory plasmas: A comparison between theory and experiment," Rev. Mod. Phys.

50, 745–795 (1978).
[24]J. F. Drake, P. K. Kaw, Y. C. Lee, G. Schmid, C. S. Liu, and M. N. Rosenbluth, "Parametric instabilities of electromagnetic waves in plasmas," The Physics of Fluids **17**, 778–785 (1974), https://aip.scitation.org/doi/pdf/10.1063/1.1694789.
[25]W. M. Manheimer and E. Ott, "Parametric instabilities induced by the coupling of high and low frequency plasma modes," The Physics of Fluids **17**, 1413–1421 (1974), https://aip.scitation.org/doi/pdf/10.1063/1.1694907.
[26]B. I. Cohen, "Compact dispersion relations for parametric instabilities of electromagnetic waves in magnetized plasmas," The Physics of Fluids **30**, 2676–2680 (1987), https://aip.scitation.org/doi/pdf/10.1063/1.866032.
[27]V. Stefan, N. A. Krall, and J. B. McBride, "The nonlinear eikonal relation of a weakly inhomogeneous magnetized plasma upon the action of arbitrarily polarized finite wavelength electromagnetic waves," The Physics of Fluids **30**, 3703–3712 (1987), https://aip.scitation.org/doi/pdf/10.1063/1.866407.
[28]T. H. Stix, *Waves in Plasmas*, 2nd ed. (Springer-Verlag New York, 1992) p. 10.
[29]C. J. Randall, J. R. Albritton, and J. J. Thomson, "Theory and simulation of stimulated brillouin scatter excited by nonabsorbed light in laser fusion systems," Phys. Fluids. **24**, 1474–1484 (1981), https://aip.scitation.org/doi/pdf/10.1063/1.863551.
[30]W. L. Kruer, S. C. Wilks, B. B. Afeyan, and R. K. Kirkwood, "Energy transfer between crossing laser beams," Phys. Plasmas **3**, 382–385 (1996), https://doi.org/10.1063/1.871863.
[31]P. Michel, L. Divol, E. A. Williams, S. Weber, C. A. Thomas, D. A. Callahan, S. W. Haan, J. D. Salmonson, S. Dixit, D. E. Hinkel, M. J. Edwards, B. J. MacGowan, J. D. Lindl, S. H. Glenzer, and L. J. Suter, "Tuning the implosion symmetry of icf targets via controlled crossed-beam energy transfer," Phys. Rev. Lett. **102**, 025004 (2009).
[32]D. J. Strozzi, E. A. Williams, D. E. Hinkel, D. H. Froula, R. A. London, and D. A. Callahan, "Ray-based calculations of backscatter in laser fusion targets," Phys. Plasmas **15**, 102703 (2008).